Isolating Solvent-Solute Hydrogen Bonding Interactions via 2D IR Solvation Shell Spectroscopy

Samuel Knight,[†,‡] Nicholas H. C. Lewis,[†,‡] Ian Bongalonta,[†,‡] John Hack,[†,‡,¶] Yumin Lee,[†,‡] and Andrei Tokmakoff[*,†,‡]

†*James Franck Institute, The University of Chicago, Chicago, Illinois, 60637, United States*

‡*Department of Chemistry, The University of Chicago, Chicago, Illinois, 60637, United States*

¶*Present Address: Department of Chemistry, University of California, Berkeley, CA 94720*

E-mail: tokmakoff@uchicago.edu

Abstract

The solvation shell around a solute is a fundamental feature of liquid-phase solutions, determining the behavior and properties of both the solute and the overall solution. Direct experimental measurements of the solvation shell properties are challenging due to the strong signals generated from the bulk solvent which overwhelm the small contribution of the solvation shell. Here, we use ultrafast two dimensional infrared (2D IR) spectroscopy and intermolecular cross-peaks to isolate the IR absorption spectrum of methanol molecules in the solvation shell surrounding the solute N-methylacetamide. We demonstrate that the intermolecular coupling between the solvent and solute vibrations is indirectly mediated by a low-frequency hydrogen-bonding mode, suggesting an important mechanism for anharmonic coupling induced by hydrogen bonds. From the relative frequency shifts and cross-peak anisotropy, we find that methanol molecules surrounding N-methylacetamide form stronger and distinctly

oriented hydrogen bonds than those in the bulk solvent. We also compare these results with the solvent spectra of the solute N,N-dimethylacetamide to investigate how solute structural changes alter the solvation shell and the contribution of N-H hydrogen bond donation. Our results are supported by molecular dynamics simulations, which provide detailed insights into the hydrogen-bonding distributions. Through these results, we demonstrate 2D solvation shell spectroscopy to be a valuable method for investigating solvation structures and dynamics without interference from the bulk solvent.

Introduction

Aqueous solvation processes influence countless phenomena in chemical science and technology, including chemical reactivity, proton and electron transfer, solubility, hydrophobicity, molecular self-assembly, chemical separations, and the numerous ways in which they influence biology.[1–6] While dielectric continuum theories can often describe solvation by aprotic solvents,[7] the behavior of solutes in water is shaped by water's dynamic hydrogen-bonding network. In particular, the organization of water molecules in the solute's first solvation shell, including the topology of water's hydrogen bonds to the solute and itself has a profound impact on the solute's conformation, solubility, and transport properties. Thus, experimental tools that allow us to understand specific water-solute interactions and track their rapid rearrangements at a molecular scale are invaluable for understanding water chemistry.

For molecular-scale solvation studies, optical and IR spectroscopy are among the most useful approaches due to their intrinsic sensitivity to molecular structure, interactions, and dynamics. Bulk spectroscopic techniques, both equilibrium and time-resolved, provide invaluable insight into solvent-solute interactions, but often rely on high solute concentrations,[8–11] spectral models,[12–14] or extrinsic probes that limit direct insight.[15–19] As the solute concentration increases, so do the desired spectroscopic signatures of solute-solvent interactions; however, this occurs in tandem with the loss of and changes to the bulk solvent and an increase in undesired solute-solute interactions. Alternatively, when observing solvent properties through a spectroscopic probe molecule,

one projects the high-dimensional solvent space onto a single coordinate, washing out information on specific solute-solvent interactions. Due to these confounding effects, a long-standing challenge in experimental studies of aqueous solvation is to isolate the properties of the solvation shell independent of the bulk solvent's influence. Sum-frequency spectroscopy accomplishes this by using symmetry breaking at interfaces as a contrast agent to isolate the response from the surface.[20–23] Spectral decomposition techniques, such as multivariate curve resolution (MCR), isolate changes in the solvent spectrum due to increasing solute concentration or other external variables.[24,25] MCR-based techniques, in particular, have been broadly successful in isolating the IR solvation shell spectrum of various solvent-solute systems.[26–29] These are useful approaches, but each has limitations: interface-specific spectroscopies are mainly restricted to large flat interfaces and are difficult to apply to molecular interfaces, while MCR and related spectroscopic models rely on user-defined constraints and the assumption of bilinear spectral components.[25]

Alternatively, spectroscopic signatures of the solvation shell can be isolated by exploiting short-range intermolecular interactions between a solute and its first solvation shell. In aqueous solutions, a natural example of such an interaction is a direct hydrogen bond between water and the solute, which produces coupling between their vibrational modes. Experimentally, hydrogen-bond mediated coupling has been observed and characterized by 2D IR spectroscopy via intermolecular cross-peaks. The initial 2D IR studies isolated this coupling for hydrogen-bonded complexes dissolved in non-polar solvents, where the solvent did not meaningfully contribute to the observed cross-peak.[30–32] Subsequent work extended this approach to water using highly charged ionic solutes that form strong hydrogen bonds with the surrounding water.[33,34] Here, we revisit this approach using a more idealized solvent-solute system that forms a modest, neutral hydrogen bond more typical of solution-phase interactions, which enables a more rigorous analysis of the information contained in intermolecular cross-peaks. Slices through the intermolecular cross-peak isolate the spectrum of the solvation shell, which, when combined with the time resolution of ultrafast spectroscopy, allows for a full characterization of the solvation shell structural dynamics. Our goal is to establish 2D IR solvation shell spectroscopy as a practical method for using intermolecular

cross-peaks to directly report on solvent-solute hydrogen bonding interactions. In this work, we test these principles and demonstrate the isolation of the solvation shell using 2D IR intermolecular cross-peaks.

To help lay the groundwork for studying aqueous solvation shells, we begin by investigating the spectroscopy of N-methylacetamide (NMA) in deuterated methanol (See chemical structure in Fig. 1(b) top inset), concentrating on the intermolecular cross-peaks between the methanol O−D stretch and the NMA amide I vibration. This solute/solvent pair has been widely studied with IR spectroscopy,[35–39] molecular dynamics (MD) simulations,[40–42,42] and electronic structure calculations,[43–45] and offers several practical benefits. Amide I vibrations (primarily C=O stretch) are particularly useful solute probes of hydrogen-bonding interactions, since their frequency red-shifts predictably by 15-20 cm^{-1} upon accepting a solvent hydrogen bond.[35,36,40] It also has a strong transition dipole moment (TDM), which assists with weak signals in 2D IR spectroscopy. At this stage we use methanol as the solvent rather than water, as it results in distinct solvent hydrogen-bonding configurations that are directly observed in the amide I IR spectrum. The IR spectra of many carbonyl molecules dissolved in methanol, including NMA, show multiple bands that correspond to 0, 1, or 2 hydrogen bonds between the carbonyl and methanol.[36,46,47] For NMA, the amide I spectrum shows two peaks assigned to the dominant populations of singly and doubly hydrogen-bonded configurations (1HB and 2HB).[36,40,48] This provides a handle to isolate these distinct solvent configurations via intermolecular cross-peaks and to study their distinctive spectroscopic signatures and intermolecular coupling. In addition, we can compare the solvent spectra of NMA with those of N,N-dimethylacetamide (DMA) (Chemical structure shown in Fig. 1(b) bottom inset) to investigate how structural modifications of the solute perturb the solvation shell and the significance of hydrogen bond donation by the amide N−H group. The focus here is on the structure of the solvation shell and a description of the solute-solvent interactions; the information on structural and vibrational dynamics in these experiments will be addressed in a subsequent paper.

We demonstrate that using intermolecular cross-peaks between the vibrations of a solute and

protic solvents is a viable approach to 2D IR solvation shell spectroscopy. These cross-peaks are measured by first exciting the methanol O−D stretch of isotopically dilute methanol and then detecting both the 1HB and 2HB amide I vibrations, to isolate distinct solvation structures. Slices through the cross-peak spectra reveal the O−D stretch spectrum of methanol solvating the NMA molecules. The relative spectral shifts of the 1HB and 2HB cross-peaks indicate that hydrogen bonds in the 1HB environment are stronger than those in both the 2HB and bulk environments, and through lineshape fitting we are able to quantify the strength of intermolecular coupling. Anisotropy measurements of the 2D cross-peak are used to characterize the orientational correlations between the hydrogen-bonded methanol O−D and amide I transition dipole moments. Finally, we compare our measurements with molecular dynamics simulations to validate our experimental conclusions. Taken together, the results clearly demonstrate the novel insights into solvation shell structure that stand to be gained from intermolecular cross-peaks while also revealing several challenges that will face ongoing investigations with this method.

Methods and Materials

Experimental

The 2D IR spectrometer used for the intermolecular cross peaks has been described extensively in previous publications,[49] but here we will provide a summary of the apparatus. In brief, the output of a 1 kHz Ti:sapphire regenerative amplifier is used to generate excitation and detection pulses in separate processes. Difference frequency generation in $AgGaS_2$ is used to produce 7 μJ pulses O−D excitation pulses centered at 2500 cm^{-1} with a bandwidth of 250 cm^{-1} FWHM and a pulse width of $\sim$50 fs. The broadband probe pulse is generated by focusing the 800 pulses along with the two following harmonics into a gentle stream of N_2 which results in a plasma that radiates broadband mid-IR pulses spanning 1,000 to 4,000 cm^{-1} with nJ pulse energy and $\sim$50 fs pulse width.[50–53]

Transient absorption and 2D IR experiments were performed with a pump-probe 2D IR spec-

trometer. The excitation pulse pair for 2D experiments is generated by sending the pump through a Mach-Zehnder interferometer, which is scanned from $\tau_1 = -350$ to 1000 fs in steps of 5 fs. Afterwards, the pump pulses are passed through a CaF_2 polarizer before focusing into the sample. After generation, the probe pulse is spatially filtered and polarized at 45° relative to the pump with a rotated silicon Brewster window before focusing it onto the sample. The relative polarization of the pump and probe pulses results in both parallel (ZZZZ) and perpendicular (ZZYY) polarization signals being generated with roughly equal intensities on the transmitted probe. To separate them, the probe is sent through a wire grid analyzer polarizer parallel to the pump which transmits ZZYY and reflects ZZZZ. The individual arms are then dispersed onto separate 64-pixel stripes of a dual-stripe mid-IR detector. The spectra were collected at two grating angles to detect the signal from ω_3 = 2000-3000 cm^{-1} and 1480-1720 cm^{-1} with a resolution of 14 and 4 cm^{-1}, respectively. For ω_3 detection frequencies below 2000 cm^{-1}, a long pass filter is used to block any second-order diffraction off the grating. The corresponding excitation axis is measured by the dark arm of the Mach-Zehnder interferometer.

The ZZZZ and ZZYY signals were measured by the change in absorbance of the probe pulse given by $\Delta A(\omega_3, \tau_2) = -\log[(S_i/R_i)(S_{i+1}/R_{i+1})]$ for a particular waiting time τ_2 between the pump and probe. Where S_i refers to the collected intensity of the probe for a given shot i, and the $i+1$ refers to the next immediate shot which is measured with the pump blocked by a 500 Hz optical chopper. R_i refers to the reference pulse which originates from the small portion of the probe pulse that is reflected off of the Si wafer and collected on an independent IR-associates single-channel detector. The isotropic (magic-angle) and anisotropy spectra were calculated with $S_{iso} = S_{ZZZZ} + 2S_{ZZYY}$ and $r = (S_{ZZZZ} - S_{ZZYY})/S_{iso}$ from the measured absorption spectra. All 2D IR spectra are shown for waiting times τ_2>100 fs to avoid a non-resonant response generated by the CaF_2 windows which would interfere with the sample's signal. Further details on signal processing and solvent background subtraction can be found in the Supplementary Information (SI) Section S1.

The 2D IR experiments used for the amide I and amide II diagonal region used a different spec-

trometer with a pump-probe 2D configuration described elsewhere.[54] The 2D spectral acquisition was similar in this case, except that both excitation and detection fields were derived from the same difference frequency generation process. The pulses were 90 fs in length, centered at 1560 cm^{-1}, and had a bandwidth was 350 cm^{-1} FWHM, which spanned the combined amide I and amide II regions. The probe beam was dispersed and detected by a 64 element array detector, resulting in a $\sim$4 cm^{-1} resolution of the detection axis.

The sample for 2D IR experiments was prepared by dissolving NMA-h_7 ($CH_3CONHCH_3$) or DMA to 1M concentration in a 15% volume mixture of CD_3OD in CH_3OH (MeOH). All samples were purchased from Sigma-Aldrich and used without further purification. At standard room temperature and pressure, NMA forms a solid that is melted before mixing with the solvent mixture. The 1M NMA concentration was chosen as an intermediate amount to avoid the well-known aggregation between individual NMA monomers,[37] but also to generate enough amide-methanol contacts for a good cross-peak signal. Hydrogen deuterium exchange (HDX) reactions result in a solution that is a mixture of the following NMA and methanol isotopologues: NMA-h_7 ($CH_3CONHCH_3$), NMA-d_1 ($CH_3CONDCH_3$), CD_3OD, CH_3OD, CD_3OH, and CH_3OH. These species have concentrations given by the following mole percentages: 3.3 : 0.6 : 2.2 : 12.7 : 12.7 : 72.3. More information of the sample composition can be found in SI Section S2. For both the linear IR and 2D IR measurements the sample was held between two 1 mm–thick CaF_2 windows with a 6 μm spacer.

Molecular Dynamics Simulations & Electronic Structure Calculations

Molecular dynamics simulations of NMA-h_7 in CH_3OH were initially performed in GROMACS 2024.3[55] using the AMBER,[56] CHARMM36m,[57] and OPLS-AA[58] force fields to compare their predictions for hydrogen bonding to the NMA carbonyl. Further characterization of the hydrogen bonding interactions were performed with AMBER. We prepared one NMA molecule with GAFF2 (v2.2.20) atom types and AM1-BCC partial charges[59] as implemented in AmberTools 24.[60] This molecule was then solvated in an orthorhombic pre-equilibrated methanol box with 10 Å

padding parameterized by AMBER's standard methanol model (MEOHBOX), resulting in a total of 211 methanol molecules. The full system was converted to GROMACS format with ACPYPE.[61] First, the system was energy minimized with with the steepest descent algorithm (max force < 100 kJ $mol^{-1}nm^{-1}$). All subsequent equilibration and production steps were performed with the leap-frog integrator with a timestep of 2 fs. Nonbonded interactions were calculated with a Verlet cutoff scheme (rlist = 1.0 nm), updating the neighbor list every 20 steps. Periodic boundary conditions were applied in all three dimensions. Electrostatics were treated with the Particle-Mesh-Ewald (PME) method[62] with a cutoff of 1.0 nm, and van der Waals interactions used the same cutoff with energy/pressure dispersion corrections. First, the system was equilibrated in NVT for 5 ns at 293 K with the velocity-rescale thermostat[63] ($\tau = 1.0$ ps) followed by NPT for 10 ns at the same temperature with the C-rescale barostat[64] at 1 bar with $\tau_p = 5.0$ ps and a compressibility of 1.214×10^{-4} bar. Production was carried out in NPT for 5 ns with the same specifications. Frames were saved every 20 fs for a total of 250000 configurations.

Hydrogen bonds were identified using the criteria described by Kwac, et al.[40] A methanol molecule was counted as hydrogen bonded to the NMA if the distance between the methanol H and the NMA acceptor O was less than $R_{O\cdots H}$= 2.5 Å and the donor-hydrogen-acceptor angle was over $\theta = 120^{\circ}$. The velocity autocorrelation function (VACF) was calculated by taking a dot product of the relative velocities between the methanol hydrogens and the NMA O atom for a given time lag and averaging over all origins and O···H pairs. Detailed equations are provided in the SI Section S3.

Vibrational anharmonicity calculations at the GVPT2 level were performed using Gaussian09RevB.01 on a system composed of a single CH_3OD molecule hydrogen bonded to the carbonyl group of a NMA-h_7 molecule embedded in a polarizable continuum solvent model for methanol. Calculations were performed with the ωB97XD functional and the 6-311G+(d,p) basis set.[65]

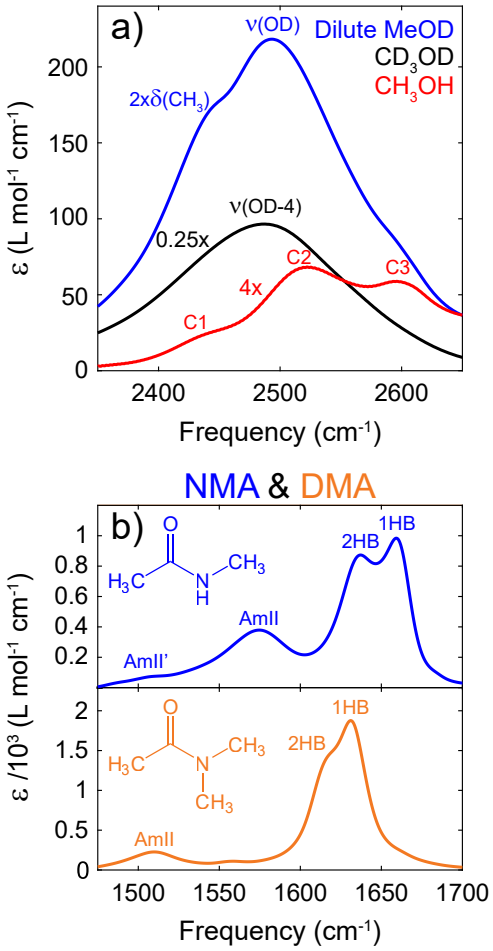

Figure 1: (a) O−D stretch spectrum of the sample (blue) compared with that for neat CD_3OD (black) and CH_3OH (red). The spectra are independently scaled for the visualization purposes (0.25xCD_3OD and 4xCH_3OH). C1, C2, C3 refer to the CH_3OH bending combination bands $\delta(\mathrm{COH}) + \nu(\mathrm{CO}), \delta(\mathrm{COH}) + \gamma(\mathrm{CH_3})$, and $\delta(\mathrm{CH_3}) + \gamma(\mathrm{CH_3})$ respectively.[66,67] (b) Solvent-background-subtracted FTIR spectra of 1M NMA (blue) and DMA (orange) in 15% isotopically dilute MeOD. The 1HB and 2HB bands are the two amide I peaks. AmII and AmII' refer to the amide II band of NMA-h_7 and NMA-d_1, respectively.

Results and Discussion

FTIR and 2D IR Spectroscopy of NMA-Methanol Solutions

To ensure that the 2D IR intermolecular cross-peak arises solely from a single hydrogen-bonded NMA-methanol pair, we used isotopically dilute methanol and optimized the NMA concentration to suppress NMA-NMA hydrogen-bonded pairs. In isotopically pure methanol, intermolecular couplings cause the O−H or O−D stretch to delocalize over multiple hydrogen-bonded molecules,[68,69]

prompting the need for isotopically dilute mixtures. Similarly at high NMA concentrations, intermolecular couplings via C=O···H−N hydrogen bonds lead to delocalization of vibrations across the NMA pairs and introduce additional solvent-solute interactions.[37] At the same time, it is also desirable to increase the concentration of MeOD and NMA as the cross-peak signal increases with the number of MeOD-NMA hydrogen bonds. Therefore, the concentrations of MeOD and NMA molecules must be optimized to balance signal strength against the ability to easily interpret the spectra.

While the concentration of MeOD is kept relatively dilute (15% CD_3OD in CH_3OH), to identify the optimal concentration of NMA that we could use without significant contamination from NMA-NMA pairs, we measured concentration-dependent FTIR spectra of NMA (Fig. S3). The spectra clearly indicate the onset of aggregation and possible NMA-NMA pairing around 5M of NMA. To maintain our sample well-below this aggregation limit, our final optimized sample is composed of 1M solution of NMA-h_7 in a mixture of 15% CD_3OD:85% CH_4OH, resulting in a mole ratio of 1 : 3.5 : 25 for NMA: MeOD: MeOH. See SI Section S2 for more details on the sample composition. The same molar ratio was prepared for the DMA sample to enable direct comparison between the spectra measured. The mixture of labile hydrogen (NMA-h_7 and CH_4OH) and deuterium (CD_3OD) atoms within the sample will result in hydrogen-deuterium exchange (HDX) between the components of the mixture. This results in several methanol and NMA isotopologues in the sample solution, which are fully explained in SI Section S2. Of the variety of different isotopologues, it is important to note that CD_3OD was the deuterium source since this results in a mixture of CD_3OD and CH_3OD in a 15%:85% ratio – we use *MeOD* to refer to both isotopologues with an O−D bond.

The FTIR spectra of the O−D stretching region for the isotopically dilute solvent is shown in Fig. 1(a) (Spectrum colored blue), along with the spectra of the solvent mixture's components (Colored black and red). The O−D stretching peak of the sample is centered at 2494 cm^{-1} and is 150 cm^{-1} wide (FWHM). The peak is flanked by a shoulder on both sides. The prominent shoulder at 2442 cm^{-1} arises from a Fermi resonance of the methyl bend $\delta(CH_3)$ with the O−D

stretch of CH_3OD.[66,67,70] The weak shoulder at 2605 cm^{-1} (peak C3) was previously assigned to methanol molecules in a specific hydrogen-bonding configuration, based on a similar IR absorption peak in solutions of CH_3OD in CCl_4.[70] Instead, we assign the peak to the CH_3OH and CH_3OD combination band, $\delta(CH_3)+\gamma(CH_3)$ (Peak C3 in Fig. 1(a)), since the peak is not present in the spectrum of CD_3OD in CCl_4 which does not contain the CH_3 combination bands (Fig. S4).

The FTIR spectrum of the amide I and amide II vibrations for NMA is shown in Fig. 1(b) (Top inset; colored blue), illustrating how unique hydrogen-bonding configurations and HDX can manifest in an IR spectrum. There are three main bands visible in the spectrum: amide I, amide II, and amide II'. The amide I (AmI) band contains distinct peaks for 1HB and 2HB solvation states that are centered at 1659 and 1637 cm^{-1}, respectively, indicating a -22 cm^{-1} shift due to the additional hydrogen bond. The AmI bands are well fit by a sum of Gaussian line shapes, the areas of which can be used to estimate the relative population of 1HB and 2HB species as $P_{1HB} : P_{2HB} = 25 : 68$ (Fig. S7). Unlike AmI, amide II (AmII) does not appear to split into distinct 1HB and 2HB peaks; instead, it is a single peak centered at 1574 cm^{-1}. Related to AmII, there is a minor peak at 1524 cm^{-1} which arises from amide II', the AmII transition from the NMA-d_1 isotopologue, indicating significant HDX between the different isotopologues. The amplitude ratio of the AmII and AmII' bands reports on the relative isotopologue populations, which suggests $\sim$15% of all NMA molecules in solution have undergone HDX (See SI Section S2 for further details). These deuterated-isotopologues have implications for the AmI vibrations as well since NMA-d_1 also contributes amide I' vibrations that are $\sim$11 cm^{-1} red-shifted from AmI and have reduced oscillator strength.[71,72] The relative red shift of both AmI' to AmI and AmII' to AmII originates from the loss of N$-$H wag character from these modes upon deuteration due to the increased bond mass and lower vibrational frequency. These red-shifted bands spectrally broaden the red side of the experimental amide I peak, potentially complicating interpretation of the peak linewidth.

The impact of N$-$H wag character and N$-$H$\cdots$O hydrogen-bonds to methanol can be further observed by studying the AmI and AmII bands of DMA (Fig. 1(b), bottom inset colored orange),

in which the nitrogen is methylated. In the DMA spectrum of AmI and AmII bands, we find the three bands to be red-shifted relative to those in NMA, with the 1HB band at 1632 cm^{-1}, the 2HB band at 1615 cm^{-1}, and the AmII band at 1510 cm^{-1}. This red shift is analogous to the shift that arises from deuteration. For both deuterated NMA and for DMA, the greater bond mass and lower vibrational frequency reduce the N−H wag character in the AmI mode. Focusing on DMA's AmI bands, there is a decreased 1HB-2HB splitting relative to NMA, down from 22 cm^{-1} to 17 cm^{-1}. This reduced splitting indicates that the methylated amide group has a decreased solvatochromic sensitivity, either from the reduced N−H wag character of AmI or missing N−H···O hydrogen-bond to methanol.[72] The AmI bands are best fit by a sum of Voigt lineshapes, the areas of which suggest that the populations of these species is roughly equal with $P_{1HB} : P_{2HB} = 48 : 46$ (Fig. S7).

While FTIR spectra are able to reveal some features of the solvation shell, 2D IR spectra are valuable for further characterizing these vibrations and isolating the interactions between them. 2D IR peaks typically appear as doublets with a ground state bleach/stimulated emission (GSB) of the fundamental transition, shown in red-yellow, and an excited state absorption (ESA) from the first excited state, which is red-shifted along the detection frequency ω_3 due to the vibrational anharmonicity and shown in blue. Figure 2 shows an overview of the isotropic 2D IR spectrum of NMA in isotopically dilute MeOD at the earliest waiting time following pulse overlap, covering the solute's amide region Fig. 2(b), the methanol O−D stretch diagonal peak Fig. 2(c), and the intermolecular cross-peak between them Fig. 2(d). This figure is displayed across the full range of the ω_1 and ω_3 axes for NMA and DMA in Figs. S8 and S9, respectively. The diagonal peaks in these areas directly correspond to the AmI, AmII, and O−D stretch peaks observed in FTIR spectra, while their cross-peaks indicate the effects of coupling between these vibrations. The intramolecular cross-peaks between AmI-AmII has been previously characterized and arises from the strong coupling between these modes.[38] While the intermolecular cross-peak arises from changes in the amide vibrations of NMA upon excitation of the methanol O−D stretch, and its presence indicates that the intermolecular hydrogen bond to the solvent results in substantial coupling between NMA and its solvation shell.

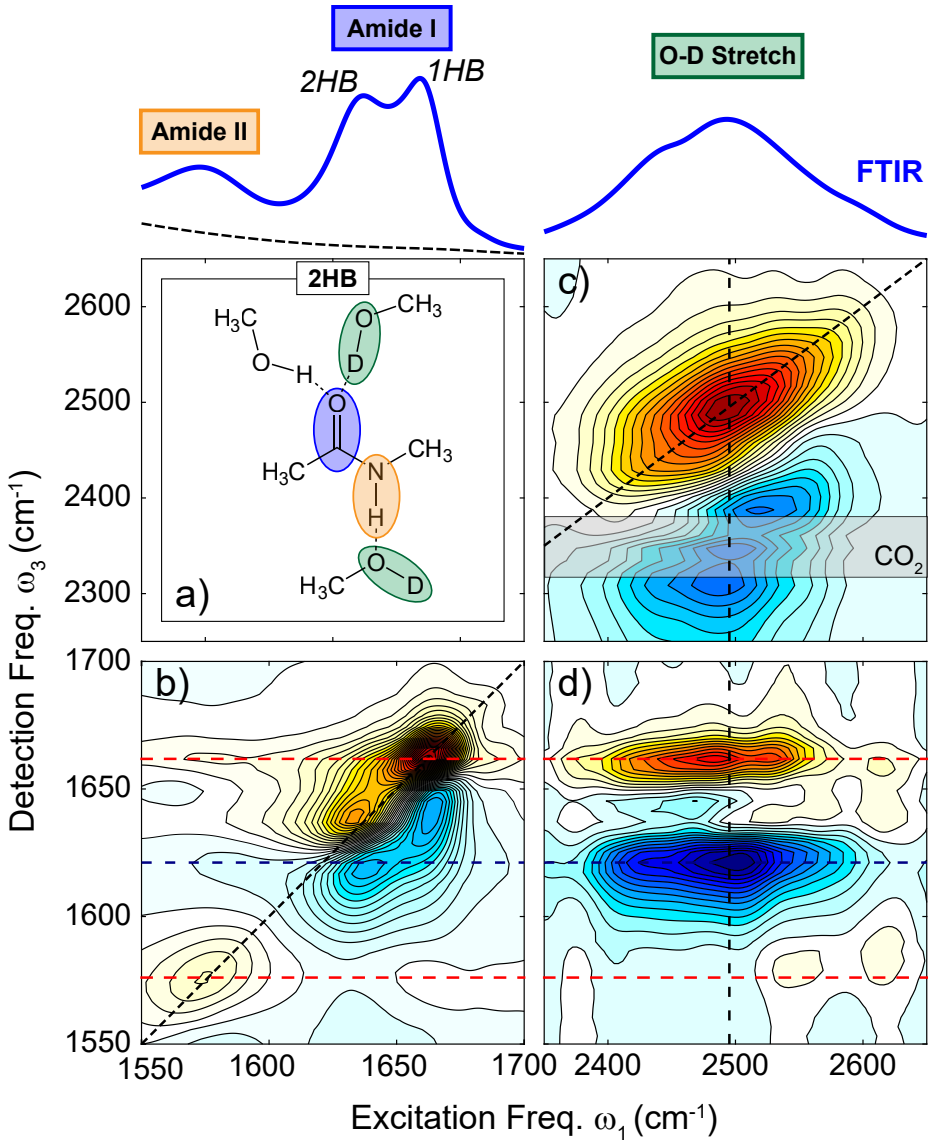

Figure 2: Isotropic 2D IR spectrum of the NMA in isotopically dilute methanol sample. The FTIR spectrum for the corresponding 2D IR spectral regions is shown above in blue. The amide I and amide II transitions are sitting on top of the tail of δ(COH) of methanol, which is shown as the black dashed line in the FTIR spectrum. (a) Example solvation structure of NMA in the 2HB configuration with the relevant vibrations colored along their dominant bonds. (b) 2D IR spectrum of the amide region taken at τ_2 = 150 fs. (c) Spectrum of the O−D stretch diagonal taken at τ_2 = 100 fs. The shaded box marks spectral interference from atmospheric CO_2. (d) Intermolecular cross-peaks between the O−D diagonal and the two amide I diagonal peaks at τ_2 = 100 fs.

The amide region of the 2D IR spectrum in Fig. 2(b) is composed of three diagonal peaks corresponding to the AmI 1HB, AmI 2HB, and AmII transitions, in addition to amide I-II cross-peaks for the 1HB and 2HB configurations. The high density of peaks within this narrow spectral

window leads to spectral congestion that complicates the interpretation. In particular, interference effects between the different peaks alter the observed intensities; specifically, the ridges along ω_3= 1660 and 1625 cm^{-1} arising from the high-frequency tail of the methanol δ(COH) absorption at 1420 cm^{-1} which extends across the entire excitation axis (see black dashed-line in FTIR inset). These intermolecular bend-stretch interactions can be quite strong, as illustrated by the strong mixing of water's H-O-H bend into AmI modes.[73] Thus, weak off-resonant excitation of the bulk MeOH bend may have a non-negligible influence on the diagonal amide I lineshape.

Comparing the 1HB and 2HB diagonal peaks at 1662 and 1635 cm^{-1}, we make two important observations regarding the ellipticity and intensity of the bands. First, the 2HB diagonal peak has a larger center-line slope (0.5) relative to the 1HB peak (0.33). This indicates greater inhomogeneity among AmI 2HB frequencies, which arises from a more diverse distribution of solvent hydrogen-bonding interactions. Second, the ratio of the 1HB to 2HB GSB peak heights (2.5) differs greatly from FTIR (1.1), even though both spectra are linearly proportional to concentration. This incongruent scaling is seen in other measurements and calculations of NMA-methanol solutions.[35,39,44] One might initially rationalize this as an effect of the differing μ^4 versus μ^2 transition dipole moment scaling of these experiments. However, applying these scaling relationships in lineshape modeling below produces unreasonable predictions for the magnitude of the 1HB transition dipole moment and the populations of the 1HB and 2HB states. This indicates some other intensity-borrowing effect by the 1HB band, and we refrain from quantitatively analyzing the peak heights. The remaining AmI cross-peak transitions seem unaffected.

Despite interference from diagonal peaks, we observe evidence for two sets of AmI-AmII cross-peaks in Fig. 2(b): uphill cross-peaks at (ω_1, ω_3) = (1550-1600, 1630-1665) cm^{-1} and downhill cross-peaks at (1630-1665, 1575-1585) cm^{-1}. The cross-peak structure is clearer when the waiting time is extended to τ_2=1 ps, as shown in Fig. 3(a) (Further waiting times shown in Fig. S10). Ideally, the cross-peaks could be better resolved by taking advantage of the 3:1 ZZZZ:ZZYY polarization amplitude ratio to subtract off the diagonal peaks from the spectrum.[48,48,74–76] However, the 3:1 ratio is accurate only for an idealized single dipole in solution and, in practice, peak

interference can reduce the measured ratio. Instead, we subtract off the diagonal peaks using a polarization ratio determined experimentally from the ratio of the diagonal peak amplitudes in the parallel and perpendicularly polarized spectra. The subtracted spectrum was calculated as $S_{sub} = 2.1S_{\perp} - S_{||}$ for τ_2=150 fs and is shown in Fig. 3(b).

The AmI-AmII cross-peaks indicate that methanol hydrogen bonding significantly modifies the strongly coupled modes and reflects associated changes in the structure of NMA. From the downhill cross-peak in Fig. 3(b), 1HB modes at $\omega_1 = 1659$ cm^{-1} correlate with AmII modes at $\omega_3 = 1578$ cm^{-1}, whereas 2HB modes at $\omega_1 = 1636$ cm^{-1} correlate with AmII modes $\omega_3 = 1586$ cm^{-1}. Thus, lower-frequency AmI modes are correlated with higher-frequency AmII modes, indicating an anticorrelated frequency shift upon hydrogen bonding to methanol. Additionally, this reveals that there are two distinct 1HB and 2HB modes of AmII as well, but they have a relatively small splitting compared to the AmI modes. Fitting the combined 1HB and 2HB downhill cross-peaks gives a slope of -0.3, showing that the AmI red shift is considerably larger than the corresponding AmII blue shift.[77] Because the AmI and AmII frequencies of NMA-h_7 scale with the C=O and N-H bond lengths, respectively,[45] these frequency correlations are directly associated with changes in NMA structure upon hydrogen-bonding with methanol. That is, adding a hydrogen bond at the carbonyl lengthens the C=O bond while also slightly shortening the N-H bond. This interplay between the structure of NMA and the hydrogen-bonding configuration can be explained by the stabilization of the zwitterionic resonance structure of NMA.[45,78,79]

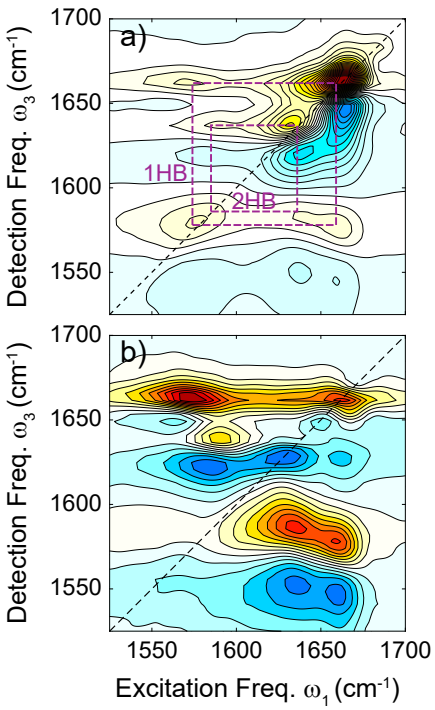

Figure 3: Anticorrelated frequency shifts in Amide I-II cross-peaks. (a) Absorptive AmI-II spectra at waiting time τ_2 = 1 ps. Corners of boxes identify the position of GSB peaks for the 1HB and 2HB species taken from the difference spectrum. (b) Difference spectrum S_{sub} at τ_2=150 fs defined in the main text.

In contrast to the amide diagonal bands, the dilute O−D stretching diagonal peak at 2500 cm^{-1} is broad and relatively featureless (Fig. 2(c)). We do observe a weak feature from the methyl-bend Fermi resonance at (ω_1, ω_3) =(2420, 2420) cm^{-1}, but its intensity is strongly suppressed by its small TDM, which similarly explains the absence of the C3 combination band discussed in the FTIR spectrum. In general, the peak exhibits the expected features of hydrogen bonding in protic solvents, namely an inhomogeneously broadened lineshape and a long-tailed ESA, which for dilute CH_3OD extends along ω_3 to $\sim$1500 cm^{-1} (Fig. S1). The inhomogeneous linewidth, with a CLS of 0.6, reflects the distribution of O−D oscillators across distinct hydrogen-bonding configurations. These hydrogen bonds are predominantly within bulk MeOH, although the 15% MeOD solution used here is not sufficiently dilute to entirely exclude the contribution of MeOD-MeOD hydrogen-bonded dimers.

Analysis of Intermolecular Cross-Peaks

The existence of OD-AmI intermolecular cross-peaks at the earliest resolvable waiting time demonstrates that the methanol O−D stretch and AmI vibration can be strongly coupled through their shared hydrogen bond, despite the large ∼850 cm^{-1} separation in frequency. This directly validates 2D IR solvation shell spectroscopy as a precise method for measuring intermolecular hydrogen-bonding between solvent and solute molecules. The presence of the instantaneous (zero-waiting time) cross peaks indicate strong anharmonic interactions that mix the modes, rather than vibrational energy transfer between two local modes.[48] The most straightforward evidence is that our TA waiting time series (Fig. S11) exhibits a monotonic population decay from zero waiting time rather than a rising cross-peak. Additionally, these cross-peaks provide direct evidence supporting the assignment of the two amide I bands as the 1HB and 2HB solvation structures. The two cross-peaks appear as a GSB at ω_3 = 1662 cm^{-1} and an ESA at 1621 cm^{-1} (Fig. 2(c)). These ω_3-frequencies correspond to the GSB of the AmI 1HB diagonal peak and the ESA of the 2HB peak, as shown by the dashed lines across Fig. 2(b) and 2(c). This indicates that both hydrogen-bonding configurations contribute a cross-peak GSB/ESA pair, but destructive interference between the 1HB ESA and the 2HB GSB suppresses the intensity between the main peaks.

To characterize the solvation shell structure, we can compare the cross-peaks of NMA and DMA both to each other and to the bulk FTIR O-D stretch spectrum. The intermolecular cross-peaks for NMA and DMA are compared in Figs. 4(a) and 4(b), where we show that both spectra have prominent GSB and ESA peaks, centered at the detection frequencies of their respective amide I 1HB GSB and 2HB ESA features. Broadly, the two sets of cross-peaks exhibit a distinct structure that is related to each molecule's unique solvation structure. The cross-peak to DMA, when compared to the cross-peak to NMA, has a greater offset in excitation frequency between the 1HB and 2HB peak frequencies (ω_1 = 2493 cm^{-1} vs. 2516 cm^{-1}), which reveals more of the underlying spectral structure. Furthermore, by taking slices through the main peaks along ω_1, we can isolate the O−D stretching spectra for the MeOD solvation shell molecules that are hydrogen bonded to NMA and DMA within the 1HB and 2HB configurations (Figs. 4(e) and 4(f)). These

methanol solvation shell spectra are clearly dominated by the broad O−D stretching mode of methanol and as a result we find there is considerable overlap between each solvent shell spectrum and the bulk methanol FTIR spectrum. There is, however, a clear difference among the individual spectra in relative frequency shifts, linewidths, and sub-band populations, the details of which provide molecular insight into the unique hydrogen-bonding configurations these peaks represent.

In comparison with DMA, the NMA cross-peak has considerably more substructure throughout the spectrum. The sub-bands may have multiple origins since the O−D stretch frequency region aligns with the N−D stretching, AmIII overtone, and combination transitions. Although the origin of any given sub-band is difficult to assign definitively, we find that almost every sub-band can be reasonably assigned to a cross-peak involving vibrations from either overtone or combination band transitions of bending modes originating from either NMA or methanol molecules. The full sub-band assignments are summarized and reported in SI Section S12. The only sub-band not originating from an overtone or combination transition is the peak at 2427 cm^{-1} in the 2HB NMA cross-peak, which originates from the excitation of a small fraction of hydrogen-bonded N−D stretches (Fig. S3(b)).

One insightful cross-peak parameter is the relative ω_1-frequency shift between the different cross-peaks and the bulk spectra, which reports on the relative strength of the distinct hydrogen bonding interactions.[80–82] In particular, we observe a relative $\sim$10 cm^{-1} red shift of the 1HB spectrum compared to the 2HB spectrum for both NMA and DMA cross-peaks (Table 1). This red shift indicates that, on average, single hydrogen bonds from methanol to NMA or DMA are stronger than those in 2HB configurations. This result is also in agreement with recent *ab initio* molecular dynamics simulations of NMA in methanol, which report two distinct O−D stretching peaks separated by 16 cm^{-1}, arising from different hydrogen bonding configurations within the solvation shell.[42] Similar agreement can be found in simulations of hydrogen-bonded water and NMA pairs, which found that as the hydrogen bond angle became more linear – a distortion one might expect when changing from a bifurcated 2HB configuration to a more linear 1HB configuration – the average O−D frequency characteristically red-shifted.[83] Now comparing to the bulk methanol FTIR

spectrum, we find both 1HB peaks of NMA and DMA exhibit a relative $\sim$5 cm^{-1} red shift to the bulk, while also exhibiting a negative skew towards redder frequencies. Meanwhile, the 2HB spectra show no consistent trends across the different metrics. In other words, hydrogen bonds between methanol and NMA or DMA may either be stronger or weaker than those in the bulk, depending on the solvent shell configuration. However, we note that because of the high density of sub-bands discussed above, there is a likely possibility that these bands could artificially produce an apparent global shift of the O-D stretching frequency. For this reason, we have restricted our interpretation to only the most prominent and reproducible features, specifically frequency shifts that are: (i) consistent between the NMA and DMA cross-peaks, despite their different sub-band populations, and (ii) agree across all frequency metrics reported in Table 1 and Fig. 4 (Peak maximum, mean frequency, and fitted center).

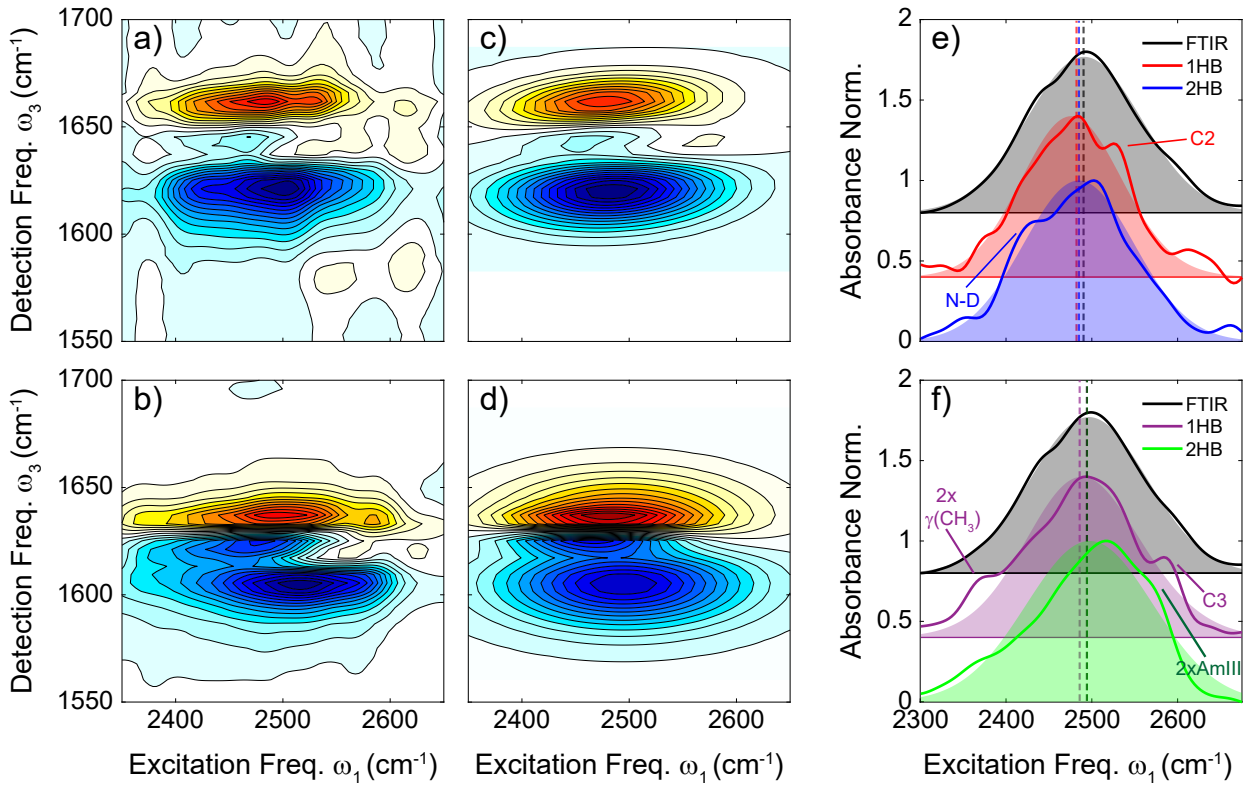

Figure 4: Intermolecular cross peaks, spectral fits, and spectral slices for 1M NMA (a, c & e) and 1M DMA (b, d, & f) in dilute MeOD. (a,b) Isotropic O−D/AmI cross-peaks at τ_2 = 100 fs. (c,d) Gaussian lineshape fits. (e,f) 1HB and 2HB slices taken along the excitation frequency through the peak maximum and minimum, respectively. Lines are the experiment and shaded regions correspond to the spectral fits from (c) and (d). Dashed lines indicate the average frequency.

Because DMA lacks an accessible N−H···O hydrogen-bonding site, whereas NMA contains one, comparing their cross-peak slices allows us to isolate the contribution of N−H···O hydrogen bonds (Figs. 4(e) and 4(f)). Both the 1HB and 2HB cross-peak slices of NMA exhibit a ∼10-15 cm^{-1} red shift relative to the corresponding slices of DMA (Table 1). This relative ω_1 red shift of both NMA cross-peaks reports a lower O−D stretching frequency for methanols hydrogen bonded to the carbonyl of NMA, indicating stronger methanol-carbonyl hydrogen bonds in the presence of N−H···O hydrogen bonds. This conclusion is consistent with electronic structure calculations, which similarly report that methanol forms stronger hydrogen bonds with the carbonyl of NMA than DMA, although by a relatively small margin.[84] Moreover, calorimetry measurements of the hydrogen-bonding enthalpies in isopropanol show that isopropanol forms stronger hydrogen bonds with NMA (-4.1 kcal/mol) than DMA (-2.4 kcal/mol),[85] a trend that is expected to carry over to methanol.

Since the formation of a methanol hydrogen bond to NMA or DMA should red-shift both the AmI and O−D stretching frequencies, one might expect the cross-peak to appear elliptical as a sign of correlated spectral broadening. However, the 1HB and 2HB cross-peak of NMA exhibit only a modest measured center-line slope of < 0.02, indicating a small decrease in AmI frequency as the O−D frequency decreases. When interpreting the correlation in cross-peaks between two vibrations with significantly different linewidths, it is important to note that even a modest correlation can result in a small, and potentially barely resolvable, slope. For example, a perfect correlation between AmI and O−D stretching frequencies, with FWHM of roughly ~ 20 cm^{-1} and ~ 150 cm^{-1} respectively, would produce a cross-peak slope of ~ 0.1. Therefore, a slope of ~ 0.02 corresponds to a correlation coefficient of 0.15, or 15%, which agrees well with the fitted correlation coefficient reported below ($\rho = 0.2 \pm 0.02$). For the DMA cross-peak, the measured center-line slope < 0.005 corresponds to a $\sim 4\%$ correlation and can be considered negligible. We believe the small center-line slopes of both solutes reflect motionally narrowed lineshapes arising from fast vibrational energy relaxation and the broad distribution of rapidly evolving hydrogen-bonding configurations, as indicated by the inhomogeneously broadened AmI and O−D diagonal

lineshapes. However, in reaching definitive conclusions, it is important to remember that low amplitude CH_3OD combination bands may distort the cross-peak lineshape.

Curiously, in Fig. 4(a), we find that NMA's AmII transition lacks cross-peaks with the O−D oscillators of the isotopically dilute MeOD, but it does share cross-peaks with the solvent CH_3OH bending combination bands at $(\omega_1, \omega_3) = (2550 - 2650, 1580)$ cm^{-1}. This absence is unexpected because NMA and MeOD form a shared N−H···O hydrogen bond, which should couple to the AmII vibration through its significant $\delta_{\text{N-H}}$ character.[86] Within the N−H···O hydrogen bond, the O−D bond of methanol is oriented off-axis from NMA's N−H bond, so that excitation of the O−D stretch by the pump pulses may induce little displacement of the N−H bond. This suggests that intermolecular cross-peaks arise only when the displacements of both vibrations are aligned along the shared hydrogen-bond axis. Given the absence of an OD-AmII cross-peak, it is surprising to find a cross-peak between AmII and CH_3OH bending combination modes, which have no immediately obvious mechanism coupling the vibrations. One possible explanation is that the NMA-to-methanol N−H···O−H hydrogen bond provides physical contact between the atoms involved in the AmII and CH_3OH bending modes, which when combined with the high concentration of CH_3OH in the sample, could produce a measurable cross-peak. Alternatively, it is possible that the cross-peak might arise from coupling between AmII and C−H bending modes of NMA itself; however, as shown in Fig. S13, there are no NMA peaks in the $\omega_1 = (2550 - 2650)$ cm^{-1} region.

Cross-Peak Lineshape Fitting

To test our interpretation of the spectra and extract vibrational coupling constants, we fit the $\tau_2 = 100$ fs MeOD-amide I cross-peak region to a Gaussian model to obtain the peak frequencies, amplitudes, and linewidths in both dimensions. The fit assumes that the 1HB and 2HB cross-peaks are both GSB/ESA doublets, with the amide I GSB frequency ($\omega_{GSB,j}$) and linewidth ($\sigma_{AmI,j}$) constrained to match the corresponding amide I peak in the FTIR spectrum (j = 1HB or 2HB). The O−D frequency and linewidth in ω_1 ($\omega_{OD,j}$ and $\sigma_{OD,j}$) and the ESA frequency in ω_3 ($\omega_{ESA,j}$) are free fitting parameters. The intensities of the ESA are softly constrained to be near harmonic

Table 1: Characterization of cross-peak spectra at $\tau_2 = 100$ fs from spectral fitting. Frequencies, linewidths, and skewness are experimental values, while values in parentheses are from the Gaussian fits to the whole cross-peak.

	Spectrum	Peak ω_{AmI} (cm^{-1})	Peak ω_{OD} (cm^{-1})	OD linewidth[1](cm^{-1})	Skewness[2]	Crosspeak Splitting, Δ (cm^{-1})
NMA	1HB	1661	2483 (2477)	171 (139)	-0.29	14.3
	2HB	1621	2502 (2483)	159 (152)	0.51	9.6
	FTIR		2490 (2489)	151 (156)	-0.15	-
DMA	1HB	1633	2493 (2469)	154 (135)	-0.53	6.5
	2HB	1625	2516 (2494)	168 (175)	-0.76	10.0
	FTIR		2494 (2494)	155 (160)	-0.41	-

[1] We report the FWHM linewidth obtained from 2.355σ where σ is the standard deviation.

[2] Calculated as $\left(\left(\langle\omega^3\rangle - \langle\omega^2\rangle\langle\omega\rangle + 2\langle\omega\rangle^3\right)/\sigma^3\right)^{1/3}$

scaling of the GSB, i.e. within ± 0.5 of the harmonic amplitude. The intensity of the cross-peak is taken to be proportional to both the fraction of 1HB or 2HB species (P_j) and the squares of the corresponding OD and AmI transition dipole moments: $A_j = P_j \mu_{OD}^2 \mu_j^2$. These parameters were also constrained to match the corresponding peaks in the FTIR spectra with $P_j \mu_j^2$ scaling. Each 2D peak was represented by a 2D Gaussian lineshape of the form

$$g_{j,\pm}(\omega_1, \omega_3) = \frac{\pm A_j}{2\pi\sigma_{OD,j}\sigma_{AmI,j}\sqrt{1-\rho^2}} \exp\left[\frac{-1}{2(1-\rho^2)}\left(\frac{\delta\omega_{1,j}^2}{2\sigma_{OD,j}^2} + \frac{\delta\omega_{3,j}^2}{2\sigma_{AmI,j}^2} - 2\rho\frac{\delta\omega_{1,j}\delta\omega_{3,j}}{\sigma_{OD,j}\sigma_{AmI,j}}\right)\right]$$

Here $+$ corresponds to GSB and $-$ to ESA, and the detunings are defined as $\delta\omega_{1,j} = (\omega_1 - \omega_{OD,j})$ and $\delta\omega_{3,j} = (\omega_3 - \omega_{j,\pm})$. The normalized covariance $\rho = \langle\delta\omega_1\delta\omega_3\rangle/\sigma_{OD}\sigma_j$ describes the extent of correlation between the frequencies and is used to fit lineshape ellipticity. Polarization constraints are included as an additional scaling term for the individual parallel and perpendicular spectra; however, this term also accounts for the pump scaling inherent to 2D IR measurements. The parallel and perpendicular spectra were fit simultaneously, only allowing the polarization scaling term to vary between the spectra. Many of the resulting fitting parameters are summarized in Table 1, and further details are presented in the SI Section S14.

Although the number of fit parameters is large, the number of constraints is sufficient that we

are able to put reasonable bounds on the parameters that quantify solute-solvent interactions. The simple lineshape model does reasonably well at capturing the broadening and interference features of the overall 2D lineshape, as seen in Figs. 4(c) and (d)) and the slices in Figs. 4(e) and 4(f). The decomposition of the lineshape into the 1HB and 2HB contributions is shown in Fig. S16 and Fig. S17 for NMA and DMA, respectively. In general, these fits are successful at identifying peak frequencies to within ± 2 cm^{-1} and obtaining accurate peak intensities, but they are less reliable for other factors. Notably, the fit indicates that the 1HB cross-peak of NMA, which had a measured CLS of ~ 0.02, is best described with a modest but significant correlation coefficient of $\rho = 0.2 \pm 0.02$, which agrees well with results obtained above from the measured slope of the 1HB cross-peak. With DMA, we cannot reliably determine this variable due to poor constraints from the FTIR spectrum.

Importantly, our fits are able to extract the cross-peak doublet splitting in ω_3, $\Delta_{ij} = (\omega_{i,GSB} - \omega_{j,ESA})$, which is used to quantify the coupling between the O$-$D stretch and AmI modes. This splitting measures the anharmonic frequency shift of the OD+AmI combination band relative to the O$-$D fundamental, and it reports on the magnitude of the intermolecular coupling introduced by the hydrogen-bonding interaction. We find that the splittings are similar for both NMA cross-peaks, 14 cm^{-1} for the 1HB and 10 cm^{-1} for the 2HB cross-peaks. For DMA, we obtain a cross-peak splitting of 6.5 cm^{-1} for the 1HB and 10 cm^{-1} for the 2HB cross-peaks – although these numbers may not be entirely accurate due to the poor fitting constraints provided from the FTIR spectrum of DMA.

To understand the intermolecular interactions that give rise to cross-peak splitting Δ_{ij}, a typical model for the coupled anharmonic vibrations would be in the form of a bilinear coupling V_{ij}.[48,87] Then, the cross peak splitting Δ_{ij} can be used together with the observed fundamental frequencies ω_i and ω_j and the diagonal peak anharmonic splittings Δ_{ii} and Δ_{jj} to determine V_{ij} through[87]

$$V_{ij}^2 = \frac{\Delta_{ij}(\omega_i - \omega_j)^2}{2(\Delta_{ii} + \Delta_{jj} + \Delta_{ij})}$$

Given diagonal splitting energies ($\Delta_{OD} \approx 150$ cm^{-1} and $\Delta_{AmI} = 13$ cm^{-1}) and the frequency difference between the O−D stretch and the two amide I peaks ($\omega_{OD} - \omega_{AmI} \approx 850$ cm^{-1}), we obtain coupling constants of $V_{OD,AmI} \approx 160$ cm^{-1} for both the 1HB and 2HB peaks. Fitting to the DMA cross-peak we obtain couplings on a similar order of magnitude. Rubstov et. al. found a similar coupling constant of 168 cm^{-1} for intermolecular N−H···O=C hydrogen bonds using a similar two-state description of the hydrogen-bond coupling.[30] However, this coupling constant is unusually high–far greater than the 5-20 cm^{-1} range of typical intermolecular vibrational couplings. To illustrate, we can estimate the transition dipole interaction between an amide carbonyl with a TDM of $0.3D$ and an hydrogen bonded O−H with a TDM of $0.05D$ that are separated by a distance of 2.5Å – and depending on orientational factors, this results in couplings <10 cm^{-1}.[48,88] Given that the direct coupling deduced from Δ_{ij} is unreasonably large, it suggests a different mechanism for the origin of the observed frequency shift than the bilinear interaction of two anharmonic normal modes. The notable factor that is omitted from this anharmonic coupling model is the hydrogen bond, therefore we sought to delineate the effect of hydrogen bonding on cross-peak splitting.

To further understand the mechanism underlying the observed cross-peak splitting, we performed vibrational anharmonicity calculations for a system composed of a single CH_3OD molecule hydrogen bonded to the carbonyl of an NMA-h_7 molecule. We found the direct anharmonic coupling between the AmI and O−D stretch normal modes to be $\lesssim 10$ cm^{-1}, which is consistent with expectations and far less than the ~ 160 cm^{-1} derived from the direct anharmonic coupling model. These smaller anharmonic couplings introduce minimal mode mixing. The O−D normal mode displacement had $\sim 1.3\%$ C=O stretch character, and the AmI mode had $\sim 2.3\%$ O−D character, a small mixing indicative of a weak interaction. We found that both modes, however, have sizable anharmonic coupling to low frequency modes with significant intermolecular character, predominantly in the hydrogen-bond O···O stretch and O−D···O bends ranging from ∼100-900 cm^{-1}. Across these modes, the O−D stretching mode was coupled with energies ranging from 15-130 cm^{-1} while the AmI was more modestly coupled by 1-5 cm^{-1}.

These observations suggest an alternative model for the OD-AmI interaction, whereby these

modes are indirectly coupled via low frequency hydrogen-bonding modes. We can test this model with a Hamiltonian for four bilinearly coupled anharmonic vibrations: the O−D stretch, AmI, AmII, and a low frequency hydrogen-bond mode (HB) that encompasses hydrogen-bond stretching or other significant intermolecular motions that influence the HB strength. The details of the coupling model are explained further in the SI Section S15. To illustrate how indirect OD-AmI coupling can produce the experimental cross-peak, we set the direct OD-AmI coupling, $\beta_{\mathrm{AmI,OD}}$, to zero and retain only the coupling of each vibration to the HB mode: $\beta_{\mathrm{HB,AmI}}$ and $\beta_{\mathrm{HB,OD}}$. Given the absence of an OD-AmII cross-peak, we also set the direct coupling of AmII with the O−D and HB modes to zero. Using non-linear least squares regression, we fit our effective Hamiltonian to match all of the experimental transition frequencies and to reproduce both the cross-peak splitting, $\Delta_{\mathrm{AmI,OD}} = 12$ cm^{-1}, and the 1HB diagonal splitting, $\Delta_{1HB} = 13$ cm^{-1}, and find values for the coupling constants of $\beta_{\mathrm{HB,AmI}} = 20$ cm^{-1} and $\beta_{\mathrm{HB,OD}} = 164$ cm^{-1}. This is sufficient to produce a cross-peak splitting of 11 cm^{-1}, give eigen energies consistent with the measured spectrum, and generate ~ 20 cm^{-1} coupling-induced frequency shifts for the O−D and AmI modes, roughly matching the experimental shifts between the 1HB and 2HB configurations. These results are consistent across a range of HB mode frequencies: 150-850 cm^{-1}, which are close to prominent peaks in the low-frequency Raman and THz spectra.[89,90] This illustrates that intermolecular cross-peaks in this case arise predominantly from hydrogen-bond displacements in distance and angle that influence the strength of the HB interaction. Such a coupling mechanism has also been proposed for similar hydrogen-bonding systems.[33,91] However, our model also predicts an OD-AmII cross-peak with the same splitting energy as the OD-AmI cross-peak, which is not consistent with the absence of this cross-peak from the measured spectrum. This inconsistency suggests that our model misses certain details about the anharmonic coupling that is producing the full observed cross-peak spectrum, and therefore, our model requires a more detailed coupling mechanism for advanced analysis.

Relative Solvent-Solute Hydrogen-Bonding Angles from 2D Anisotropy

The intermolecular cross-peak can also provide insight into the molecular geometry of the hydrogen-bonded methanol-amide pair through polarization-dependent studies. For this analysis we computed the 2D anisotropy, r, of the intermolecular cross-peak from the parallel and perpendicular polarized 2D spectra (Fig. 5). While the intensity changes between parallel and perpendicular spectra (Figs. 5(b), 5(c)), overall, the 2D lineshape of NMA does not vary much and retains most of the substructure described above. The 2D anisotropy characterizes the relative orientations of μ_a, the transition dipole moment (TDM) excited at frequency ω_1, and μ_b, the TDM detected at frequency ω_3 after a waiting time τ_2. Assuming a separation of vibrational and rotational degrees of freedom and negligible orientational motion during τ_1 and τ_3, the anisotropy can be approximated by

$$r(\tau_2) = \frac{2}{5}\langle P_2[\hat{\mu}_{\mathrm{a}}(0) \cdot \hat{\mu}_{\mathrm{b}}(\tau_2)]\rangle. \tag{1}$$

Here, the caret designates a unit vector, P_2 is the second-order Legendre polynomial, and $\langle \ldots \rangle$ is an orientational average over the directions of the two TDMs. A value of $r = 0.4$ indicates that $\hat{\mu}_a$ and $\hat{\mu}_b$ are parallel, whereas $r = 0$ reflects uncorrelated orientations or a relative angle of 54.7°.

The 2D cross-peak anisotropies of NMA and DMA at the shortest waiting time (τ_2 = 100 fs) are shown in Figs. 5(a) and 5(d). At these early waiting times, which are short compared to orientational relaxation, the AmI and O-D TDMs retain partial orientational correlation, yielding anisotropy values of $r \approx 0.15$-0.2 at each peak's maximum. A finite anisotropy value implies a nonzero angle between the O−D stretch and AmI TDMs, providing a potential route to extract the relative hydrogen-bonding geometries. However, relating a measured anisotropy value to a specific hydrogen-bond angle is not straightforward. First, the TDMs do not lie directly along the bonds of interest (Fig. 6) which must be corrected for. In addition, a distribution of hydrogen-bond geometries leads to a spread of relative TDM angles, α, further complicating the interpretation of a single anisotropy value. For these reasons, we do not analyze the absolute anisotropies here.

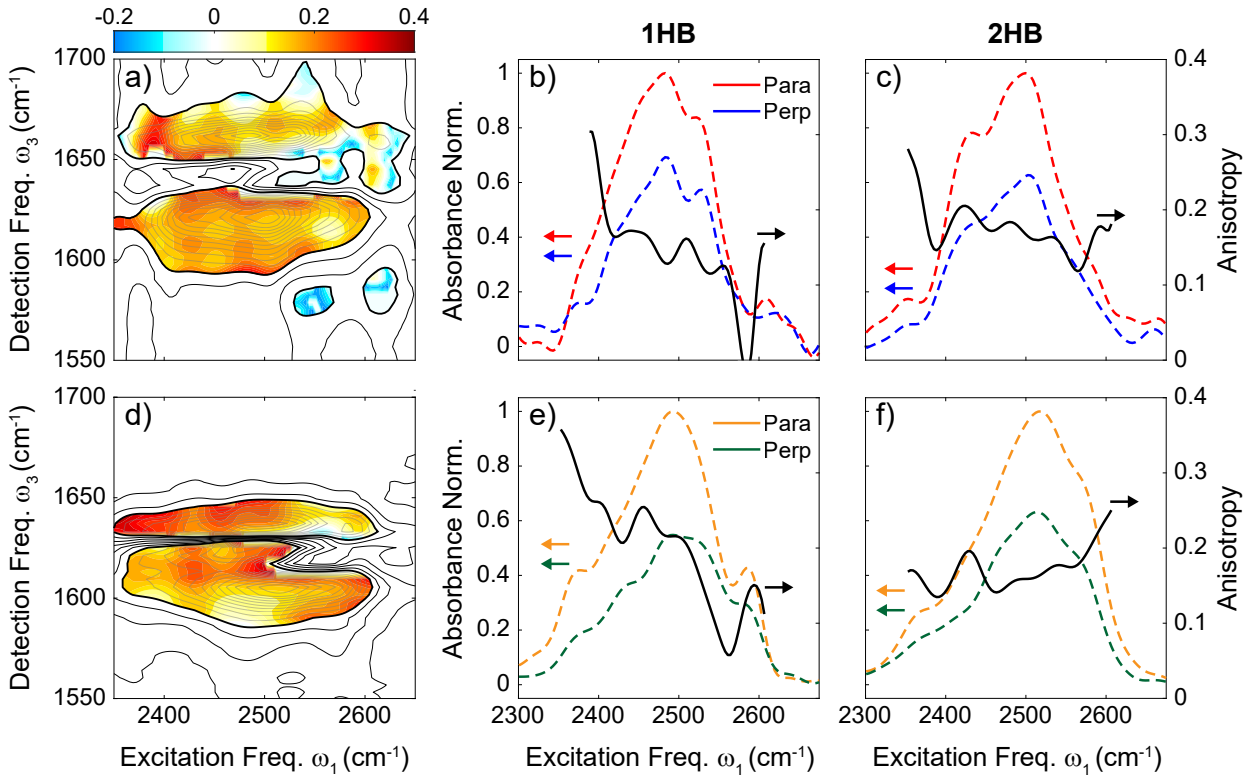

Figure 5: (a) 2D cross-peak anisotropy for NMA at τ_2 = 100 fs. To avoid uncertainty within low intensity regions, anisotropy values above 0.4 and less than -0.2 are not plotted. 1HB (b) and 2HB (c) slices taken through the respective ω_3 extrema of the parallel and perpendicular cross-peak spectra. The black lines correspond to the anisotropy. The same 2D cross-peak anisotropy plots for DMA (d) and 1HB (e) and 2HB (f) are also plotted.

Instead, we introduce analytical models below that enable a quantitative connection between the measured anisotropy and the hydrogen-bonding geometry.

Looking more closely at the anisotropy trends of the polarized spectra in Figs. 5(b) and 5(c), these cross-peak slices demonstrate how anisotropy is correlated to hydrogen bond strength. The band with the largest variation in anisotropy is the 1HB peak of DMA (Fig. 5(e)), which increases from 0.1 to 0.3 with decreasing ω_1-frequency. This variation is consistent with general expectations from hydrogen bonding, increasing the strength of a hydrogen bond simultaneously downshifts the O−D frequency and makes the bond more linear, thereby increasing the anisotropy. Within the 1HB band of NMA (Fig. 5(b)) we see a similar anisotropy trend; the lowest ω_1-frequencies, $\omega_1 < 2400$ cm^{-1}, show a sharp increase in anisotropy to 0.3. However, although this is similar in trend to the DMA 1HB anisotropy, the two may not have the same origin as the large anisotropy

value is also consistent with the excitation of the NMA N-D stretch TDM, $\hat{\mu}_{ND}$, that lies parallel to the AmI TDM, $\hat{\mu}_{AmI}$. As for the 2HB anisotropy trends of NMA and DMA, there is no robust trend across both cross-peaks so we refrain from making any definitive conclusions.

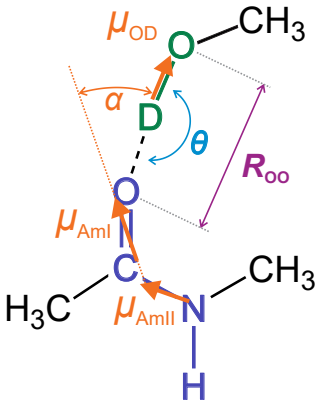

Figure 6: Configurational variables for the NMA-methanol hydrogen bond and transition dipole moments (in orange). R_{OO} is the O···O hydrogen bond length, θ is the O−D···O hydrogen bond angle and α is the AmI-OD transition dipole projection angle

Models for Interpreting the Cross-Peak Anisotropy

We aim to gain insight into the hydrogen-bond orientation from analysis of the anisotropy. In the case of a rigid body, descriptions of the orientational averages and correlation functions that contribute to 2D IR cross-peaks have been used to establish the relationship between r and the fixed angle between TDMs, α, where $\hat{\mu}_{\mathrm{a}} \cdot \hat{\mu}_{\mathrm{b}} = \cos\alpha$.[74–76,92] The anisotropy in the absence of orientational dynamics is

$$r(\alpha) = \frac{1}{5}(3\langle\cos^2\alpha\rangle - 1). \tag{2}$$

While r may provide information on the relative TDM angle (α), this is not a direct insight into the hydrogen-bonding angle. Hydrogen-bonding angles (θ in Fig. 6) describe the angle between the donor and acceptor bonds, independent of their TDMs. When describing the relationship of the anisotropy to the hydrogen-bonding angles of NMA, we must account for the orientation of $\hat{\mu}_{AmI}$ relative to the C=O bond ($\sim 20^\circ$) shown in Fig. 6.[38]

Connecting the cross-peak anisotropy to the underlying methanol hydrogen-bonding configurations is not straightforward. While there may be preferential hydrogen-bonding configurations for the 1HB and 2HB species, one also expects considerable variation in α from a distribution of possible hydrogen-bonding angles. Using models, we can establish an explicit relationship between the anisotropy and the statistics of α, providing a basis for interpreting our experiments. To explicitly account for variations in the alignment of $\hat{\mu}_a$ and $\hat{\mu}_b$, we must average over a specified angular probability density. These models, the response functions, and the orientational averages are described fully in SI Section S16.

First, we consider the hard-cone model, a minimalist model that illustrates the ambiguity between a fixed relative angle and a finite-width angular distribution underlying a measured anisotropy value. Within the hard-cone mode, the relative TDM angle α is uniformly distributed within a cone of polar angle $\delta\theta$ centered on the parallel orientation of $\hat{\mu}_a$ and $\hat{\mu}_b$ ($\alpha = 0$) as illustrated in Fig. 7(a).[93,94] The orientationally averaged anisotropy is then calculated as

$$r_{hc} = \frac{1}{5}\cos\delta\theta\,(\cos\delta\theta + 1). \tag{3}$$

Comparing the variations in anisotropy with fixed angle, α, to the variation in anisotropy as a function of cone angle $\delta\theta$ in Fig. 7(c) illustrates the ambiguity associated with interpreting a given value of the anisotropy. In these two limiting cases, the anisotropy of 0.17 can be interpreted as arising from fixed hydrogen bonding configurations with an angle of α = 38° or as a uniform distribution of angles with a cone angle of $\delta\theta$ = 57°. Of course, a combination of smaller average values of α and $\delta\theta$ would also produce the same anisotropy. As a result, additional constraints are needed to uniquely assign these two variables, as has been shown in polarization-dependent SFG measurements.[95,96]

To describe the angular probability densities for the 1HB and 2HB configurations, our model must account for simultaneous variations in the fixed relative angle and angular width, such as the "tilted cone" model from ref. 97. Here, we investigate a simpler model in which the probability

density for α in spherical coordinates is centered on the polar angle θ_0 and distributed uniformly within a range of angles $\pm\delta\theta$ about θ_0 in both θ and ϕ (Fig. 7(c)). For this "tilted pyramid" distribution, the orientational average of α over spherical angles results in

$$r_{tp} = \frac{1}{5}(4\cos^2\theta_0\cos^2\delta\theta - \cos^2\theta_0 - \cos^2\delta\theta). \tag{4}$$

when $\theta_0 + \delta\theta < \pi$ and $\theta_0 > \delta\theta$. When $\delta\theta \to 0$ this gives back eq. 2. When $\delta\theta > \theta_0$, we recover the hard cone model (eq. 3) with the replacement $\delta\theta \to \theta_0 + \delta\theta$. The behavior predicted by eq. 4 is illustrated in figure 7(d), with contours indicating how a given value of the anisotropy may arise from different values of θ_0 and $\delta\theta$. If we consider an anisotropy of $r = 0.17$ and assert that the average angle between the $\hat{\mu}_{OD}$ and $\hat{\mu}_{AmI}$ transition moment is bent, such as we anticipate for the 1- and 2HB states, this model indicates that θ_0 is no larger than 38° and $2\delta\theta = < 113°$. Ideally, performing an additional measurement sensitive to the orientational distribution function would allow us to uniquely specify the center angle, θ_0 as well as the angular width $\delta\theta$. However, even without further constraints, the intermolecular anisotropy will prove helpful for comparison with the orientational distributions predicted by different MD force fields.

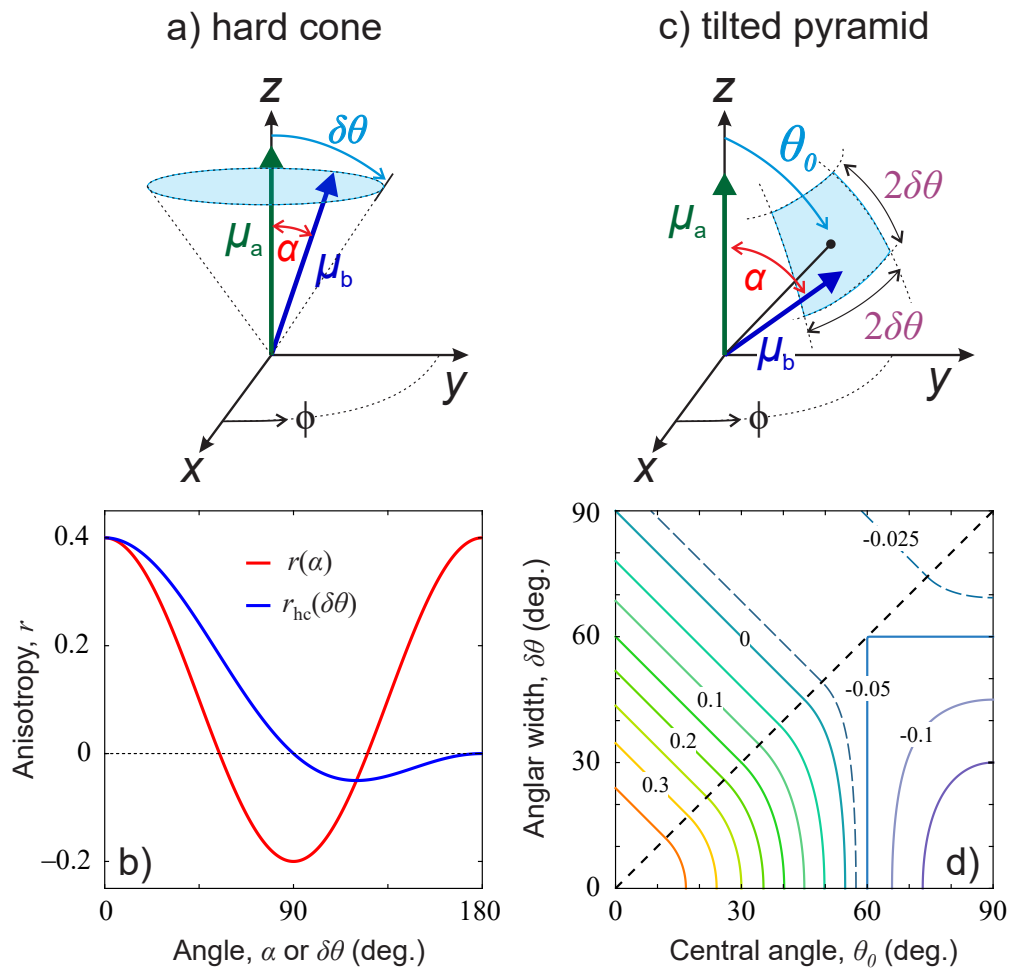

Figure 7: Modeling the impact of orientational distributions on cross-peak anisotropy. For two dipoles, α is the relative (polar) angle between two transition dipole moments $\hat{\mu}_a$ and $\hat{\mu}_b$ in the body-fixed frame. (a) The hard cone angle models uniform distributions of α, within a cone of angle $\delta\theta$ centered on $\hat{z}$. (b) Calculated anisotropy for two fixed dipoles subtending an angle α (eq. 2, red), or widening the distribution of angles $\delta\theta$ about $\theta_0 = 0$ for a hard cone model (eq. 3, blue). (c) The tilted pyramid orientational distribution functions $P(\theta_0, \delta\theta)$ are specified by the average angle θ_0 and $\delta\theta$, the width of angles allowed with equal probability about θ_0 in θ and ϕ. (d) Anisotropy from the tiled cone model as function of θ_0 and $\delta\theta$ (eq. 4).

Molecular Dynamics Simulations

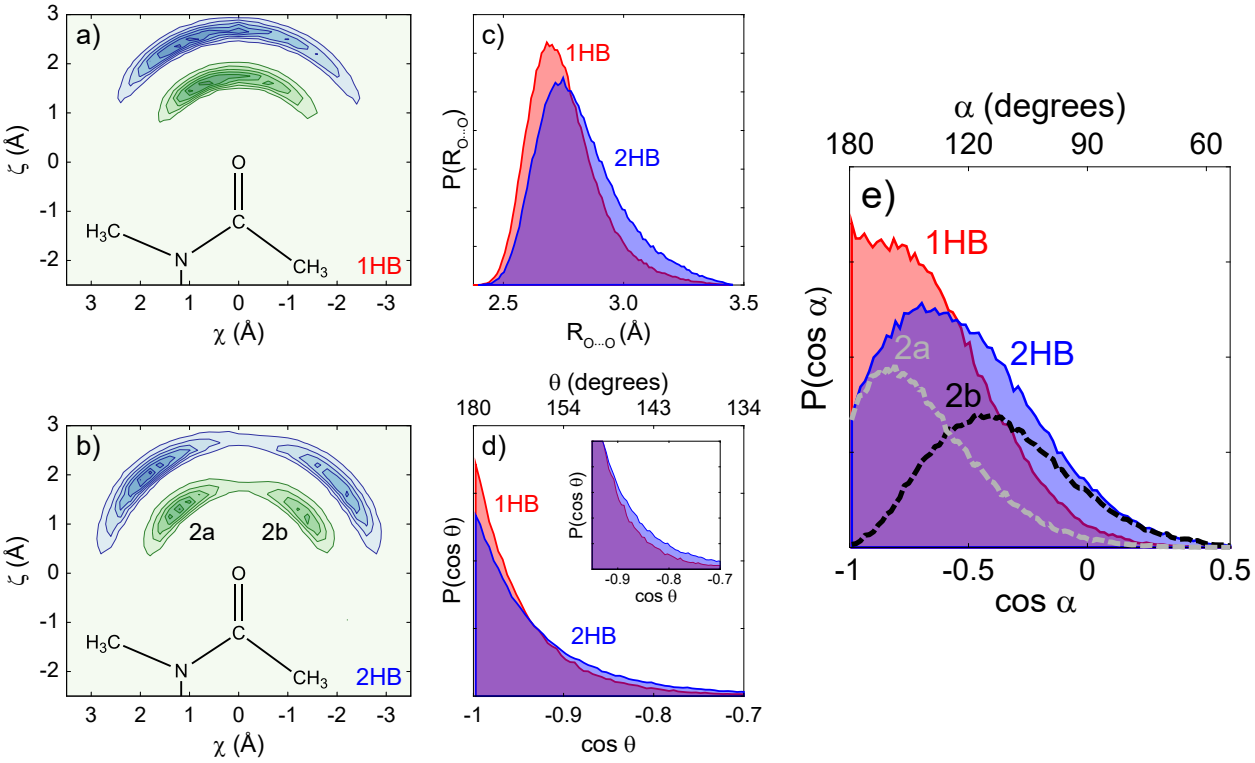

Figure 8: Probability distribution functions (PDFs) and solvent density taken from molecular dynamics simulations. The solvent density in (a) and (b), for 1HB and 2HB respectively, show the methanol hydrogen (green) and oxygen (blue) densities in a modified Cartesian coordinate system (χ, ζ) defined in the main text and SI section S16.1. The atomic structure of NMA is shown on the plot and is positioned to the atomic coordinates of the simulated NMA structure. The PDFs for the 1HB (red) and 2HB (blue) configurations for (c) donor-acceptor oxygen-oxygen distance $R_{\mathrm{O\cdots O}}$, (d) O−D···O hydrogen-bonding angle θ, and (e) relative TDM angle α. We chose to express both angular probability densities as a function of $\cos\theta$ or $\cos\alpha$ rather than the pure angles to remove the angular dependence from the spatial volume used to calculate the density.[81]

To help interpret our experimental results in terms of hydrogen-bonding configurational ensembles, we performed classical molecular dynamics (MD) simulations of NMA in methanol. The simulations allow us to directly visualize the solvent shell and extract hydrogen-bonding parameters that are directly related to the intermolecular cross-peak. In particular, we calculated the probability distribution functions (PDFs) that characterize the geometry of the O−D···O hydrogen-bond distance and angle, which are related to the hydrogen-bond strength and thus the ω_1-frequency of the cross-peaks. Additionally, we can calculate the PDF for the $\hat{\mu}_{OD}$-$\hat{\mu}_{AmI}$ TDM angle using the Jansen

dipole map,[44] which is directly related to our 2D anisotropy measurements. The agreement between the MD simulations and our experiment depends strongly on the force field (See Table 2 and the discussion section below). Among the three force fields tested: AMBER, CHARMM36m, and OPLS-AA; AMBER reproduced the experimental 1HB:2HB population ratio (0.54:0.43) reported by our FTIR data and is in good agreement with the earlier simulations by Kwak and Cho using the AMBER/parm99 force field.[40] In contrast, CHARMM36m and OPLS-AA reported population ratios significantly different from the experiment (Table 2). As a result, we continue our analysis solely with the AMBER force field.

Table 2: Percent of configurations in MD trajectory of three force fields corresponding to 0, 1, 2, and 3 O−H···O hydrogen bonds between the methanol O−H and the NMA carbonyl. The hydrogen bond criterion is $R_{\mathrm{H\cdots O}} < 2.5$Å and $\theta > 120^{\circ}$

Force Field	0 HB	1 HB	2 HB	3 HB
AMBER	2.6	56.4	39.7	1.3
CHARMM36m	10.0	67.0	22.4	0.6
OPLS-AA	33.4	57.3	9.1	0.2

We visualize the solvation shell through the spatial density of methanol oxygen and hydrogen atoms in the 1HB (Fig. 8(a)) and 2HB (Fig. 8(b)) configurations. The densities are plotted in a modified Cartesian coordinate system (χ, ζ) where the green and blue colors indicate methanol hydrogens and oxygens, respectively. In this representation, Θ is defined as the angle between the methanol O−H bond and the NMA C=O bond. We chose this flattened 2D coordinate system because simple projections of the 3D methanol density onto a 2D Cartesian plane can result in the appearance of nonphysical hydrogen-bonding distances and overlapping NMA and methanol molecules. Within this coordinate system, the relative distances and angles can be interpreted as normal, although they are not strictly Cartesian. The coordinate system is defined further in SI Section S17.

In the 1HB (Fig. 8(a)) and 2HB (Fig. 8(b)) configurations, the methanol molecules form distinct hydrogen-bonding geometries with NMA. The 1HB configuration is centered near the NMA oxygen, whereas the 2HB configuration clusters into two partially overlapping positions on either

side of the NMA carbonyl. We label the position at positive χ as **2a** and that at negative χ as **2b**. Given their overlapping density, to quantitatively extract the hydrogen-bonding parameters of the 2HB angular distribution, we fit the 2a and 2b peaks to a sum of two Gaussian functions (See Fig. S20). The hydrogen-bonding parameters of 1HB configuration report a nearly linear hydrogen-bond between methanol and the NMA carbonyl, $\langle\Theta_{1HB}\rangle = 5.5^{\circ}$, whereas the **2a** and **2b** hydrogen bonds are tilted away from the carbonyl, with $\langle\Theta_{2a}\rangle = 43.0^{\circ}$ and $\langle\Theta_{2b}\rangle = -46.4^{\circ}$. As an ensemble, the 2HB configuration spans a slightly wider range of hydrogen-bonding angles than the 1HB configuration, consistent with the general conclusions from the AmI diagonal measurements discussed above. However, for a single methanol molecule the opposite is true. A methanol molecule in the 1HB configuration samples a broad angular range about its mean orientation ($\sigma_{1HB} = 33.5^{\circ}$), whereas in the 2HB configuration it is confined to either the 2a or 2b geometry, each with much narrower angular fluctuations ($\sigma_{2a} = 20.4^{\circ}$, $\sigma_{2b} = 20.7^{\circ}$). Therefore, while the 2HB ensemble appears broader because it comprises of two distinct orientations, each individual methanol in the 2HB configuration is more tightly constrained than in the 1HB configuration

To test our experimental conclusions about the relative hydrogen-bond strength between the 1HB and 2HB configurations, we analyze the corresponding structural and angular PDFs from the MD simulation. The structural PDF in Fig. 8(c) shows the probability distribution functions of oxygen-oxygen hydrogen-bond lengths, $R_{\mathrm{O\cdots O}}$, for the 1HB and 2HB configurations. Comparing these PDFs reveals that the most probable hydrogen bond lengths are 2% longer in 2HB configurations (2.82 Å) than in 1HB (2.75 Å) configurations, indicating weaker hydrogen bonds in the 2HB configuration. These relative changes are consistent with the 1% AmI and 0.6% O−D stretching frequency down-shifts upon formation of an additional hydrogen bond, which scale proportionally with bond length.[45,98] The small magnitude of these changes indicates that methanol–NMA hydrogen bonds are weak overall, but systematically weaker in the 2HB than in the 1HB configuration, in agreement with the cross-peak analysis.[99] Consistent with this picture, the hydrogen-bond angular PDFs in Figure 8(d), show that although both configurations are nearly linear on average, the angular distribution is narrower for 1HB (σ^2_{1HB} = 0.004) than 2HB (σ^2_{2HB} = 0.006), again in-

dicating weaker hydrogen bonds in the 2HB configuration. Together, both the radial and angular PDFs support our conclusion from the experiment that hydrogen bonds are modestly weaker in the 2HB configuration than in the 1HB configuration.

Table 3: Hydrogen bonding configuration statistics for 1HB and 2HB configurations in MD simulations with AMBER

	Population	$\langle R_{O\cdots O}\rangle$ (Å)	$\langle\cos\theta\rangle$	$\langle\cos\alpha\rangle$	r
1HB	0.564	2.753	-0.942	-0.643	0.087
2HB	0.397	2.818	-0.924	-0.510	0.013

As discussed above, the 2D anisotropy reflects both the fixed TDM angle and the spread of TDM orientations arising from the distribution of hydrogen-bonding geometries, captured by the tilted-pyramid model. To test this interpretation, we plot in Fig. 8(e) the PDF of $\cos(\alpha)$, which describes the TDM angle between $\hat{\mu}_{AmI}$ and $\hat{\mu}_{OD}$. In particular, the PDF-averaged TDM angle, $\langle\cos\alpha\rangle$, is the quantity most directly related to the measured cross-peak anisotropy, r. It depends on both the most probable TDM angle and variance in TDM angle, which corresponds in the tilted pyramid model to the fixed TDM angle (θ_o) and angular width ($\delta\theta$), respectively. For the 1HB and 2HB PDFs, the most probable TDM angles differ significantly from one another, the 1HB distribution peaks at a linear TDM angle, $\cos\alpha = -1$, while the 2HB distribution peaks at a bent TDM angle, $\cos\alpha = -0.70$. Taken alone, these peaks would suggest very different anisotropy values. However, both distributions are sufficiently broad (Table 3) that their average TDM is much closer, with $\langle\cos\alpha\rangle = -0.64$ for 1HB and $\langle\cos\alpha\rangle = -0.51$ for 2HB, generally consistent with the similar 1HB and 2HB cross-peak anisotropy values. This behavior illustrates the same interplay between the fixed angle and angular width embodied in the tilted-pyramid model and motivate its usage for interpreting cross-peak anisotropy measurements.

To quantitatively compare the anisotropy predicted from the TDM PDF in Fig. 8(e) to the experimental anisotropy values, we calculate the anisotropy using equation 2 and obtain: $r_{1HB} = 0.087$ and $r_{2HB} = 0.013$. The calculated anisotropy deviates significantly from the experimental value of $r \approx 0.17$ determined for both 1HB and 2HB cross-peaks. The discrepancy could be caused by factors in either method, namely, the simulated distributions may not accurately reflect

the experiment, or perhaps the spectral congestion in the experiment may be artificially modifying the measured anisotropy value. However, we believe the former is correct and the experiment is more accurate of the real anisotropy since the measured anisotropy is similar for both NMA and DMA cross-peaks, in spite of their different degrees of spectral congestion, suggesting the measurement is robust.

Assignment of the Hydrogen Bonding Mode

Finally, as a way of interpreting the low frequency hydrogen bonding mode that mediates the intermolecular vibrational interactions, we computed a density of states for the hydrogen bond mode from a velocity autocorrelation function (VACF). We calculated the VACF as $\langle \delta \mathbf{v}_{HB}(t) \delta \mathbf{v}_{HB}(0) \rangle$ with $\delta \mathbf{v}_{HB} = \mathbf{v}_{HB}(t) - \langle \mathbf{v}_{HB}(t) \rangle$, defining the differential velocity between the NMA oxygen and CH_3OH hydrogen as the vector $\mathbf{v}_{HB} = \dot{r}_O - \dot{r}_H$. The resulting VACF shows pronounced underdamped beats (Fig. 9(a)) which, upon computing the Fourier transformation, result in a density of states spectrum with a prominent peak at 254 cm^{-1} and smaller bands at 133 cm^{-1} and ~ 600 cm^{-1} (Fig. 9(b)). These match the measured low-frequency Raman and Terahertz spectra of pure methanol.[89,90] The 600 cm^{-1} mode is well established as the librational band of CH_3OH, while the 133 and 254 cm^{-1} modes exhibit mixed hydrogen bond translational and librational character, suggesting a similar origin for the HB mode in our model.[90,100] Relating to our model Hamiltonian, this range of frequencies is also well within the frequency range of plausible HB modes (150-850 cm^{-1}) with which our model Hamiltonian can produce physically meaningful spectral energies. Similarly, this frequency range is consistent with the vibrational frequencies calculated by our vibrational anharmonicity calculations above.

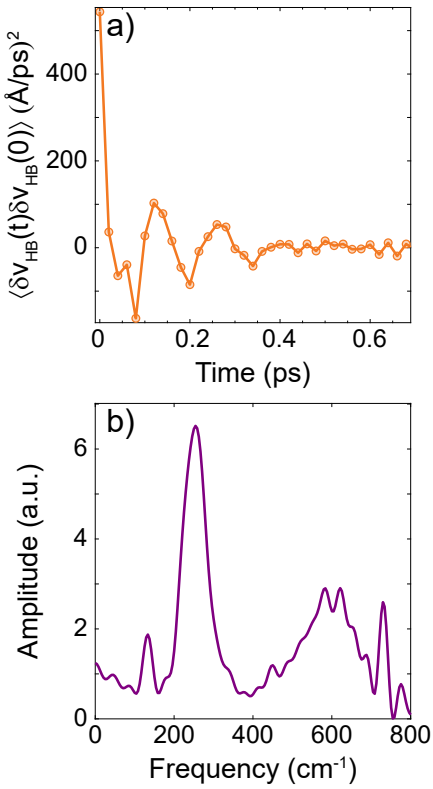

Figure 9: Determining the intermolecular hydrogen-bonding mode using molecular dynamics simulations. (a) The velocity autocorrelation function (VACF) $\langle \delta v_{HB}(t) \delta v_{HB}(0) \rangle$, where v_{HB} is defined in the main text and SI section S3.2. The time points were sampled at 20 fs intervals. (b) The vibrational density of states calculated by Fourier transforming the VACF.

Discussion

Considerations for Observing Intermolecular Cross-Peaks

As our study has illustrated, there are a number of design considerations that can significantly change the information content accessible in 2D IR solvation shell spectroscopy and intermolecular cross-peaks. Practically, we encountered challenges from both the sample we chose, i.e. significant HDX from isotopically dilute mixtures and relatively small spectral shifts, and from our experimental-design choices, specifically the measured spectral region and use of downhill cross-peaks, which introduce strong spectral congestion from overtone vibrations and solvent background signals. While the challenges relating to the system weren't too severe in this work, our

experimental-design could be reasonably questioned. For example, exciting the dilute O−H stretch near 3400 cm^{-1} instead of the O−D stretch at ∼2500 cm^{-1} would avoid the spectral congestion of the bending overtones, but also would introduce much stronger interference from the AmI and AmII overtones near 3300 cm^{-1} and 3150 cm^{-1}, respectively. Therefore, removing unwanted spectral congestion requires carefully selecting solute and solvent isotopologues to shift unwanted peaks out of the measured spectral window, together with careful background subtraction. Additionally, using the uphill rather than the downhill cross-peak would also be undesirable, because of distortions in the O−D stretch cross-peak from strong interference along the ω_3-axis originating from the large anharmonicity of the O−D stretch.

Beyond these practical considerations, there are also important conceptual challenges when choosing the intermolecular cross-peak. The molecular insight obtainable from the intermolecular cross-peaks depends significantly on the nature of the two vibrations studied. For instance, in many systems the solute vibrational bands are not split into distinct peaks originating from different steady-state solvent configurations, as we've seen here for NMA and DMA in methanol. Rather, in such systems the vibrational frequency is averaged across many different solvation environments and as a result distinct cross-peaks for the unique states will not be present at the earliest waiting time, but instead, emerge at longer waiting times due to chemical exchange between the distinct solvent environments.

Hydrogen-Bond Mediated Intermolecular Coupling and the Origin of the Cross-Peak

While the existence of the 1HB and 2HB cross-peaks demonstrates that a single hydrogen bond suffices to couple a solvent and solute vibration, our modeling revealed that both vibrations must be indirectly coupled to the intermediate hydrogen-bonding mode for there to be an observable cross-peak. Thus, hydrogen-bond mediated interactions appear to be an important mechanism in studying the solvation shell in polar protic solvents. Conversely, we are unable to observe a cross-peak to AmII at early τ_2 for the case of NMA, even though NMA and MeOD participate

in a shared N−H···O hydrogen bond, which should interact with the AmII vibration because of its pronounced δ(N−H) contribution. This absence can be understood from the geometry of the N−H···O hydrogen bond: the O−D bond of MeOD is oriented off-axis relative to NMA's N−H bond, such that displacements of the O−D stretch must not efficiently drive the hydrogen bond mode. Thus, even through MeOD participates in the hydrogen bond, its O−D stretching vibration is not directly aligned with the N−H···O coordinate. This suggests that it is necessary to align two hydrogen-bonded vibrations along the shared hydrogen-bond axis to produce significant intermolecular cross-peaks. Consequently, weaker or off-axis couplings between vibrations that are not directly involved in the hydrogen bond may be difficult to detect though intermolecular cross-peaks. This is particularly interesting to consider with the bulk O−H stretching mode of isotopically pure water, which is delocalized across many water molecules due to significant intermolecular coupling induced by hydrogen bonding.[69,101] Given the significance of the direct hydrogen-bonding mode for intermolecular cross-peaks, it is not clear whether an intermolecular cross-peak between O−H in isotopically pure water and a hydrogen-bond acceptor would report on each coupled water molecule or only the O−H stretch directly hydrogen bonded to the solute. Alternative direct coupling mechanisms, such as transition dipole coupling, would require the solute and solvent vibrations to be relatively well matched in frequency to observe their interactions and produce relatively small 10-20 cm^{-1} coupling energies.

The role of hydrogen bond modes in mediating intermolecular coupling can be anticipated from the hydrogen-bonded O−H stretching vibrations in water and in strongly hydrogen-bonded complexes. Extensive literature has established that coupling between the O−H stretch and hydrogen bonds modulates the O−H stretching frequency as the hydrogen bonds dynamically evolve.[101–105] A similar coupling occurs for the AmI mode, with its vibrational frequency likewise sensitive to hydrogen-bonding.[35,36,39,40] Strong intermolecular coupling has also been isolated for strongly hydrogen-bonded complexes through intermolecular cross-peaks in 2D IR spectra.[30–32,106] Such hydrogen-bond induced intermolecular coupling is highly anharmonic, as expected from the multidimensional potential energy surfaces that describe water-water hydrogen bonding, ranging from

the empirical Lippencott-Schroeder potential to highly accurate many-body potential energy surfaces.[107–109] What we have observed here is that the same hydrogen bonding mediates intermolecular interactions with the far less anharmonic vibrations of a hydrogen-bond acceptor. In the case of amides, these low frequency modes influence this coupling by modulating the hydrogen bond distance which influences electrostatic couplings, the shifting of zwitterionic character in the amide group, and orbital overlap that results in charge transfer from the carbonyl oxygen to the methanol proton.[45,79,110] These interactions combined are strong enough to be observed as cross-peaks. While our results here emphasize indirect coupling via a hydrogen bond mode as the dominant mechanism, there may be some contribution from direct solute-solvent coupling that cannot be entirely excluded and will require further modeling to quantify accurately.

Relative Populations of Distinct Hydrogen-Bonding States

The relative population of the 1HB and 2HB configurations can be obtained to first order from fitting the 1HB and 2HB AmI bands in FTIR spectra, which give $(P_{1HB}, P_{2HB}) = (0.25, 0.68)$ for NMA and $(0.48, 0.46)$ for DMA. More accurate fractions are obtained by accounting for the slight variation in the TDM for 1HB and 2 HB species since the integrated FTIR absorbance scales with $|\mu_j|^2 P_j$. Computations have found that the AmI TDM decreases with frequency by $\sim 1\%$ per 1cm^{-1},[111] which allows us to calculate that $(P_{1HB}, P_{2HB}) = (0.31, 0.55)$ for NMA and $(0.53, 0.36)$ for DMA. The values for DMA compare favorably to previous molecular dynamic simulations,[40] and the simulations above using AMBER. The population difference between NMA and DMA stems from NMA's complex FTIR lineshapes, where strong AmI-AmII coupling and the presence of AmI' oscillators from HDX broaden the measured linewidths and artificially shifts the reported populations. A more accurate model-independent method for determining the relative populations would be to compute the peak amplitude ratios between the 2D IR, which scales as $|\mu_j|^4 P_j$, and FTIR, which scales as $|\mu_j|^2 P_j$, spectra. This provides the necessary constraints to determine both μ_j and P_j.[112–115] Unfortunately, the 1HB peak amplitude in the 2D IR spectrum is enhanced by an as-yet-unknown intensity borrowing mechanism, which precludes this analysis.[112]

Notably, the different simulations, summarized in Table 2, predict the existence of a significant population of NMA molecules in a non-hydrogen bonded (0HB) configuration. This raises the question of whether we can detect such a configuration in our experimental AmI spectra. Within the IR spectrum, we'd expect such a peak to occur at the highest AmI frequencies due to the $\sim$15-20 cm^{-1} blue shift AmI vibrations experience upon loosing a hydrogen bond. Looking at the AmI FTIR spectrum for both NMA and DMA (Fig. 1), there is a shoulder in both spectra on the high-frequency side of the 1HB band, potentially from a small 0HB population. Furthermore, the 2D IR spectrum indicates the shoulder is a distinct peak, showing a small diagonal peak at a similar frequency at select waiting times (Fig. S10). There is also precedence for a 0HB state found in similar IR studies of ester carbonyls in methanol which exhibited a much more pronounced three peak structure than seen here for NMA and DMA, which was assign to the 0-, 1-, and 2HB configurations.[116,117] Based on these observations and our population analysis above, we conclude that there are three observable solvent configurations (0HB, 1HB, and 2HB) and estimate that the fraction of 0HB species for NMA and DMA to be <10%.

Molecular Insights into the 1HB and 2HB Solvation Shell Configurations

Analyzing the relative O$-$D stretching frequencies of the 1HB, 2HB, and bulk spectra, we find for both NMA and DMA that the 1HB spectrum is red-shifted relative to both the 2HB ($\sim$10-20 cm^{-1}) and bulk ($\sim$5 cm^{-1}) spectra. This indicates that methanol forms the strongest hydrogen-bonds in the 1HB configuration, although the difference is modest. Such small shifts should be analyzed with caution since the O$-$D stretch spectra have a broad linewidth and high spectral congestion. However, the small difference between the 1HB and 2HB hydrogen-bond strengths is reproduced in both our simulations above and recent ab-initio studies, although these calculations disagree with our conclusion of weak bulk hydrogen bonding.[42] In further support of this small energetic difference, our temperature-dependent FTIR spectra of the 1HB and 2HB peaks (Fig. S21) reveal small ($\sim$0.1 %) increases in the population of 1HB with temperature. A van't Hoff analysis of this population change yields an enthalpy difference of $\Delta H_{HB} \lesssim 2$ kJ/mol between the two solvent

configurations. A consistent estimate follows a Badger-Bauer analysis of the 1HB and 2HB spectra, which relates O−D stretch frequency shifts to changes in hydrogen-bond enthalpy on order of $\Delta H_{HB}/\Delta\omega \approx 0.1$ (kJ mol^{-1})/cm^{-1}. Applying this relation to the ∼10-20 cm^{-1} red shift of the 1HB-2HB spectra gives $\Delta H_{HB} \approx 1-2$ kJ/mol, which agrees well with the estimates from the van't Hoff analysis.[118–120]

The 5-15 cm^{-1} red shift of the NMA solvation shell spectra relative to DMA suggests that hydrogen bonds to the N−H group of an amide strengthens hydrogen bonds at the carbonyl. The key insight is that this strengthening of the carbonyl hydrogen bond arises from hydrogen bonding at a different site, where formation of an N−H···O hydrogen bond on NMA enhances the ability of the carbonyl to accept a hydrogen bond from methanol. Therefore there is a cooperative coupling between distinct hydrogen-bonding sites across the NMA molecule.[77,110] Such cooperative hydrogen bonding is enabled by the strong interaction between the polarizing hydrogen bond and the zwitterionic structure of NMA.[45,71,79] For example, in the N−H···O hydrogen bond between NMA and methanol, the proximity of the negatively charged methanol oxygen to the positively charged hydrogen in the N−H bond stabilizes the charged state of NMA, thereby promoting the formation of a second hydrogen bond with the solvent. In support of this mechanism, electronic structure calculations have shown that, in response to a N−H hydrogen bond, the structure of NMA changes and there is an AmI red shift of 10 cm^{-1}.[79] However, other calculations report a smaller shift (<2 cm^{-1}).[77]

Finally, for our anisotropy measurements we can directly validate our tilted pyramid model for the measured anisotropy through comparisons to the calculated TDM angular PDF. Through both methods, we interpret the measured anisotropy of 0.15-0.2 for NMA and DMA originating from a combination of distinct hydrogen-bonding angles (θ_o) and a significant variance in possible hydrogen-bonding angles ($\delta\theta$). To determine the accuracy of the tilted pyramid model, we compare the anisotropy calculated directly from the 1HB TDM PDF using eq. 2 with the anisotropy predicted by the tilted pyramid model based on the reported mean and width of the distribution. From the 1HB TDM PDF the calculated anisotropy is $r_{1HB} = 0.087$. The tilted pyramid model, us-

ing a mean of $\langle\alpha\rangle = 50^\circ$ and standard deviation of $\sigma = 75^\circ$ (calculated from arccosine of the mean and standard deviation in $\cos\alpha$-space) predicts $r_{1HB} = -0.049$. This discrepancy shows the tilted pyramid model is nonphysical and does not truly reflect the underlying TDM distribution. This is not surprising as molecular systems are described by continuous distribution functions that do not typically contain discontinuous hard-wall cut-offs inherent to the tilted pyramid model. While the model fails to predict accurate TDM distributions, it provides a useful analytical tool for analyzing trends in anisotropy while accounting for variations in both average angles and angular widths.

Conclusion

Two-dimensional IR solvation shell spectroscopy and the analysis of intermolecular cross-peaks provide us with quantitative insight into hydrogen-bonding interactions between methanol and NMA, including the strength, geometry, and vibrational coupling of the shared hydrogen bonds. More specifically, early-time intermolecular cross-peaks encode these properties in three spectral observables: relative frequency shifts (Hydrogen-bond strength), anisotropy (Relative TDM angles), and the GSB-ESA splitting (Vibrational coupling). In total, the information we have revealed about the methanol solvation shell around NMA is generally consistent with the picture that has developed from prior experiments and simulations of NMA in methanol and water, along with a handful of new insights. However, we note that a full characterization of all these variables is made possible with 2D IR solvation shell spectroscopy.

As a technique, 2D IR solvation shell spectroscopy fills a gap among existing spectroscopic methods for probing solvation structure by selectively reporting on solvent-shell localized vibrational spectra. These spectra provide direct sensitivity to changes in molecular structures, interactions, and dynamics within specific solvation motifs. In this way, the technique compliments other powerful spectroscopies such as IR and Raman solvation shell spectroscopy,[24,28] which measure the vibrational spectrum of the entire solvation shell but cannot resolve distinct solvation structures. However, a key limitation is that 2D IR solvation shell spectroscopy relies on significant

inter-molecular couplings and consequently, weak solvent-solute interactions, such as the free O-H groups around hydrophobic moieties, will likely not be detected. Experimentally, the technique requires independent control of the detection and excitation pulse frequencies to capture the distinct vibrational frequencies of the solvent and solute. This is typically achieved using two mid-IR sources generated by optical parametric amplification followed by difference frequency generation. Here, we eliminate the need to tune the detection frequency altogether by employing a broadband detection pulse, which detects spectral changes across the entire mid-IR in response to excitation at a particular vibrational frequency.[49,50,121]

2D solvation shell spectroscopy and its intermolecular cross-peaks enable a wide range of new experimental directions. In particular, early-time intermolecular cross-peaks offer two powerful capabilities that were not explored here, namely high spectral contrast from their unique detection frequencies, and direct measurement of solvent-shell populations through their amplitudes. The latter benefit is especially valuable, as it allows one to accurately track changes in chemical equilibria alongside spectral signatures of molecular-scale structure. These observables will be particularly interesting to monitor to see how specific solvation motifs respond to a controlled perturbation. Water, in particular, exhibits a rich structural diversity around ions, hydrophobic solutes, and macromolecules. In these systems, the perturbations may be molecular, such as changes in solute charge distribution or hydrophobicity, or macroscopic, such as variations in temperature or pressure, which drive the solvation shell to new thermodynamic states by altering its hydrogen-bonding configuration.

At the same time, there is also exciting future research to be done with MD simulations in conjunction with 2D IR solvation shell experiments. As shown here, the structural distributions obtained from MD simulations are extremely helpful in interpreting our experimental results and suggest the promise of more elaborate analysis. In particular, future calculations may extract static configurations and distribution functions to help further clarify the amide-methanol hydrogen-bonding interactions and solvation structures. Furthermore, dynamical analysis using correlation functions based on hydrogen bond numbers and orientational vectors could be used to determine

hydrogen-bond lifetimes and orientational correlation timescales for the 1HB and 2HB solvent shells. Direct comparison with experiment can be accomplished by calculating the intermolecular cross-peak spectrum from simulation, for example, by combining conventional O-H/D and AmI spectral maps with the methanol-amide hydrogen-bonding distribution functions and associated conditional probabilities.[86] This comparison would be particularly useful for confirming that the cross-peak spectra truly originate solely within the amide solvation shell. With our current results, we can only provide a rationale based on the short-ranged vibrational coupling of a hydrogen bond and the use of a dilute solvent mixture.

While this study focuses on the solvent shell structure, waiting time dependent intermolecular cross-peaks will reveal dynamic information about the solvation shell. Specifically, these measurements will extend the structural insights from short-time cross-peaks to the dynamics of hydrogen bonding and energy dissipation between the coupled modes. These topics and more will be explored in a future publication. This promises 2D IR solvation shell spectroscopy to be a valuable method for investigating novel solvation shell structure and dynamics.

Supplementary Information

The supplementary information contains: a description of the isotopic composition of the sample, the full FTIR data analysis, 2D IR data over the full spectral range acquired for ZZZZ and ZZYY polarization at 100 fs, representative waiting time spectra, details for processing 2D data, full assignments for the cross-peak sub-bands, additional results from the cross-peak fitting, a full description of all models used (Anharmonic coupling Hamiltonian and anisotropy distribution models), a Van't Hoff analysis of temperature-dependent FTIR spectra, and details of MD simulation and statistics for the hydrogen bonding distances and angles for 1HB and 2HB configurations.

Acknowledgments

This work was supported by the Department of Energy, Office of Science, Basic Energy Sciences under grant DE-SC0014305. NHCL acknowledges support through the Advanced Materials for Energy-Water Systems (AMEWS) Center, an Energy Frontier Research Center funded by the U.S. Department of Energy, Office of Science, Basic Energy Sciences, under Contract No. DE-AC02-06CH11357. I.B acknowledges support from the National Science Foundation Graduate Research Fellowship Program under Grant No. DGE-2140001. Any opinions, findings, and conclusions or recommendations expressed in this material are those of the authors and do not necessarily reflect the views of the National Science Foundation. The molecular dynamics simulations were performed with the computational resources provided by the University of Chicago Research Computing Center. We thank Artemie Chang and Anuj Pennathur for helpful comments and edits on the manuscript.

References

(1) Hynes, J. T. Chemical Reaction Dynamics in Solution. *Annual Review of Physical Chemistry* **1985**, *36*, 573–597.

(2) Ball, P. Water as an Active Constituent in Cell Biology. *Chemical Reviews* **2007**, *108*, 74–108.

(3) Garrett, B. C. et al. Role of Water in Electron-Initiated Processes and Radical Chemistry: Issues and Scientific Advances. *Chemical Reviews* **2004**, *105*, 355–390.

(4) Southall, N. T.; Dill, K. A.; Haymet, A. D. J. A View of the Hydrophobic Effect. *The Journal of Physical Chemistry B* **2002**, *106*, 521–533.

(5) Pratt, L. R. Molecular Theory of Hydrophobic Effects: "She is too mean to have her name repeated.". *Annual Review of Physical Chemistry* **2002**, *53*, 409–436.

(6) Berne, B. J.; Weeks, J. D.; Zhou, R. Dewetting and Hydrophobic Interaction in Physical and Biological Systems. *Annual Review of Physical Chemistry* **2009**, *60*, 85–103.

(7) Nitzan, A. *Chemical Dynamics in Condensed Phases: Relaxation, Transfer, and Reactions in Condensed Molecular Systems*; Oxford University Press: New York, NY, 2006.

(8) Fulfer, K. D.; Kuroda, D. G. Ion speciation of lithium hexafluorophosphate in dimethyl carbonate solutions: an infrared spectroscopy study. *Physical Chemistry Chemical Physics* **2018**, *20*, 22710–22718.

(9) Hung, S. T.; Roget, S. A.; Zheng, W.; Fayer, M. D. Concentration Dependence of Dynamics and Structure among Hydrated Magnesium Ions: An Ultrafast Infrared Study. *The Journal of Physical Chemistry B* **2023**, *127*, 3278–3290.

(10) Carpenter, W. B.; Lewis, N. H. C.; Fournier, J. A.; Tokmakoff, A. Entropic barriers in the kinetics of aqueous proton transfer. *The Journal of Chemical Physics* **2019**, *151*, 034501.

(11) Pan, J.; Charnay, A. P.; Fica-Contreras, S. M.; Fayer, M. D. Restricted Orientation Anisotropy Method for FVE Radii Characterization: Confirmed and Refined via the Study of Six Vibrational Probes. *Macromolecules* **2024**, *57*, 903–915.

(12) Hendler, R. W.; Shrager, R. I. Deconvolutions based on singular value decomposition and the pseudoinverse: a guide for beginners. *Journal of Biochemical and Biophysical Method* **1993**, *28*.

(13) Widjaja, E.; Garland, M. Pure component spectral reconstruction from mixture data using SVD, global entropy minimization, and simulated annealing. Numerical investigations of admissible objective functions using a synthetic 7-species data set. *Journal of Computational Chemistry* **2002**, *23*, 911–919.

(14) Fayer, M. D.; Levinger, N. E. Analysis of Water in Confined Geometries and at Interfaces. *Annual Review of Analytical Chemistry* **2010**, *3*, 89–107.

(15) Fica-Contreras, S. M.; Daniels, R.; Yassin, O.; Hoffman, D. J.; Pan, J.; Sotzing, G.; Fayer, M. D. Long Vibrational Lifetime R-Selenocyanate Probes for Ultrafast Infrared Spectroscopy: Properties and Synthesis. *The Journal of Physical Chemistry B* **2021**, *125*, 8907–8918.

(16) Lim, C.; Jeon, J.; Park, K.; Liang, C.; Chae, Y.; Kwak, K.; Cho, M. Revisiting Ultrafast Dynamics in Carbonate-Based Electrolytes for Li-Ion Batteries: Clarifying 2D-IR Cross-Peak Interpretation. *The Journal of Physical Chemistry B* **2023**, *127*, 9566–9574.

(17) Gasse, P.; Stensitzki, T.; Müller-Werkmeister, H. M. 2D-IR spectroscopy of azide-labeled carbohydrates in H2O. *The Journal of Chemical Physics* **2024**, *161*.

(18) Jimenez, R.; Fleming, G. R.; Kumar, P. V.; Maroncelli, M. Femtosecond solvation dynamics of water. *Nature* **1994**, *369*, 471–473.

(19) Rosenthal, S. J.; Jimenez, R.; Fleming, G. R.; Kumar, P.; Maroncelli, M. Solvation dynamics in methanol: Experimental and molecular dynamics simulation studies. *Journal of Molecular Liquids* **1994**, *60*, 25–56.

(20) McDermott, M. L.; Vanselous, H.; Corcelli, S. A.; Petersen, P. B. DNA's Chiral Spine of Hydration. *ACS Central Science* **2017**, *3*, 708–714.

(21) Guyot-Sionnest, P.; Hunt, J.; Shen, Y. Sum-frequency vibrational spectroscopy of a Langmuir film: Study of molecular orientation of a two-dimensional system. *Physical Review Letters* **1987**, *59*, 1597–1600.

(22) Scatena, L. F.; Brown, M. G.; Richmond, G. L. Water at Hydrophobic Surfaces: Weak Hydrogen Bonding and Strong Orientation Effects. *Science* **2001**, *292*, 908–912.

(23) Strazdaite, S.; Versluis, J.; Backus, E. H. G.; Bakker, H. J. Enhanced ordering of water at hydrophobic surfaces. *The Journal of Chemical Physics* **2014**, *140*, 054711.

(24) Ben-Amotz, D. Hydration-Shell Vibrational Spectroscopy. *Journal of the American Chemical Society* **2019**, *141*, 10569–10580.

(25) De Juan, A.; Jaumot, J.; Tauler, R. Multivariate Curve Resolution (MCR). Solving the mixture analysis problem. *Anal. Methods* **2014**, *6*, 4964–4976.

(26) Long, J. A.; Rankin, B. M.; Ben-Amotz, D. Micelle Structure and Hydrophobic Hydration. *Journal of the American Chemical Society* **2015**, *137*, 10809–10815.

(27) Mochizuki, K.; Ben-Amotz, D. Hydration-Shell Transformation of Thermosensitive Aqueous Polymers. *The Journal of Physical Chemistry Letters* **2017**, *8*, 1360–1364.

(28) Sun, Y.; Petersen, B. P. Solvation Shell Structure of Small Molecules and Proteins by IR-MCR Spectroscopy. *The Journal of Physical Chemistry Letters* **2017**, *8*, 611–614.

(29) Casalini, E.; Stingel, A. M.; Moussa, B.; Personeni, M.; Petersen, P. B.; Verde, A. V. Hydrophilic–Hydrophobic Double Layers around Amphiphilic Solutes in Mixed Solvents. *JACS Au* **2025**, *5*, 2992–2999.

(30) Rubtsov, I. V.; Kumar, K.; Hochstrasser, R. M. Dual-frequency 2D IR photon echo of a hydrogen bond. *Chemical Physics Letters* **2005**, *402*, 439–443.

(31) De Marco, L.; Thämer, M.; Reppert, M.; Tokmakoff, A. Direct observation of intermolecular interactions mediated by hydrogen bonding. *The Journal of Chemical Physics* **2014**, *141*, 034502.

(32) Stingel, A. M.; Petersen, P. B. Couplings Across the Vibrational Spectrum Caused by Strong Hydrogen Bonds: A Continuum 2D IR Study of the 7-Azaindole–Acetic Acid Heterodimer. *The Journal of Physical Chemistry B* **2016**, *120*, 10768–10779.

(33) Fournier, J. A.; Carpenter, W.; De Marco, L.; Tokmakoff, A. Interplay of Ion–Water and Water–Water Interactions within the Hydration Shells of Nitrate and Carbonate Directly

Probed with 2D IR Spectroscopy. *Journal of the American Chemical Society* **2016**, *138*, 9634–9645.

(34) Lewis, N. H. C.; Dereka, B.; Zhang, Y.; Maginn, E. J.; Tokmakoff, A. From Networked to Isolated: Observing Water Hydrogen Bonds in Concentrated Electrolytes with Two-Dimensional Infrared Spectroscopy. *The Journal of Physical Chemistry B* **2022**, *126*, 5305–5319.

(35) Woutersen, S.; Mu, Y.; Stock, G.; Hamm, P. Hydrogen-bond lifetime measured by time-resolved 2D-IR spectroscopy: N-methylacetamide in methanol. *Chemical Physics* **2001**, *266*, 137–147.

(36) Eaton, G.; Symons, M. C. R.; Rastogi, P. P. Spectroscopic Studies of the Solvation of Amides with N-H Groups. *Journal of the Chemical Society Faraday Transactions* **1989**, *85*, 3257–3271.

(37) Salamatova, E.; Cunha, A. V.; Bloem, R.; Roeters, S. J.; Woutersen, S.; Jansen, T. L. C.; Pshenichnikov, M. S. Hydrophobic Collapse in N-Methylacetamide–Water Mixtures. *The Journal of Physical Chemistry A* **2018**, *122*, 2468–2478.

(38) Deflores, L. P.; Ganim, Z.; Ackley, S. F.; Chung, H. S.; Tokmakoff, A. The Anharmonic Vibrational Potential and Relaxation Pathways of the Amide I and II Modes of N-Methylacetamide. *The Journal of Physical Chemistry B* **2006**, *110*, 18973–18980.

(39) Decamp, M. F.; Deflores, L.; McCracken, J. M.; Tokmakoff, A.; Kwac, K.; Cho, M. Amide I Vibrational Dynamics of N-Methylacetamide in Polar Solvents: The Role of Electrostatic Interactions. *The Journal of Physical Chemistry B* **2005**, *109*, 11016–11026.

(40) Kwac, K.; Lee, H.; Cho, M. Non-Gaussian statistics of amide I mode frequency fluctuation of N-methylacetamide in methanol solution: Linear and nonlinear vibrational spectra. *The Journal of Chemical Physics* **2004**, *120*.

(41) Kwac, K.; Cho, M. Molecular dynamics simulation study of N-methylacetamide in water. I. Amide I mode frequency fluctuation. *The Journal of Chemical Physics* **2003**, *119*.

(42) Yadav, V. K.; Klein, M. L. Probing the dynamics of N-methylacetamide in methanol via ab initio molecular dynamics. *Physical Chemistry Chemical Physics* **2017**, *19*, 12868–12875.

(43) Karplus, H. G.; Martin Ab Initio Studies of Hydrogen Bonding of Af-Methylacetamide: Structure, Cooperatlvlty, and Internal Rotational Barriers. *Journal of Physical Chemistry* **1992**, *96*, 7273–7287.

(44) La Cour Jansen, T.; Knoester, J. A transferable electrostatic map for solvation effects on amide I vibrations and its application to linear and two-dimensional spectroscopy. *The Journal of Chemical Physics* **2006**, *124*, 044502.

(45) Hayashi, T.; Zhuang, W.; Mukamel, S. Electrostatic DFT Map for the Complete Vibrational Amide Band of NMA. *The Journal of Physical Chemistry A* **2005**, *109*, 9747–9759.

(46) Pazos, I. M.; Ghosh, A.; Tucker, M. J.; Gai, F. Ester Carbonyl Vibration as a Sensitive Probe of Protein Local Electric Field. *Angewandte Chemie International Edition* **2014**, *53*, 6080–6084.

(47) Max, J.-J.; Chapados, C. Infrared spectroscopy of acetone-methanol liquid mixtures: Hydrogen bond network. *The Journal of Chemical Physics* **2005**, *122*, 014504.

(48) Hamm, P.; Zanni, M. *Concepts and methods of 2D infrared spectroscopy*; Cambridge University Press, 2011.

(49) Hack, J. H.; Lewis, N. H. C.; Knight, S.; Carpenter, W. B.; De Marco, L.; Ramasesha, K.; Tokmakoff, A. Generation and Implementation of Continuum Infrared Pulses for Broadband Detection in 2D IR Spectroscopy. *The Journal of Physical Chemistry A* **2024**, *128*, 4901–4910.

(50) Petersen, P. B.; Tokmakoff, A. Source for ultrafast continuum infrared and terahertz radiation. *Optics Letters* **2010**, *35*, 1962.

(51) Ramasesha, N. C. C.-F.; Knepper, R.; Wood, M.; Krupa Sub-picosecond to Sub-nanosecond Vibrational Energy Transfer Dynamics in Pentaerythritol Tetranitrate. *The Journal of Physical Chemistry Letters* **2020**, *11*, 6664–6669.

(52) Ramasesha, N. C. C.-F.; Knepper, R.; Wood, M.; Krupa Mode-Selective Vibrational Energy Transfer Dynamics in 1,3,5- Trinitroperhydro-1,3,5-triazine (RDX) Thin Films. *The Journal of Physical Chemistry A* **2021**, *125*, 7788–7802.

(53) Stingel, A. M.; Petersen, P. B. Full spectrum 2D IR spectroscopy reveals below-gap absorption and phonon dynamics in the mid-IR bandgap semiconductor InAs. *The Journal of Chemical Physics* **2021**, *155*, 104202.

(54) Ashwood, B.; Lewis, N. H. C.; Sanstead, P. J.; Tokmakoff, A. Temperature-Jump 2D IR Spectroscopy with Intensity-Modulated CW Optical Heating. *The Journal of Physical Chemistry B* **2020**, *124*, 8665–8677.

(55) Abraham, M. J.; Murtola, T.; Schulz, R.; Páll, S.; Smith, J. C.; Hess, B.; Lindahl, E. GROMACS: High performance molecular simulations through multi-level parallelism from laptops to supercomputers. *SoftwareX* **2015**, *1-2*, 19–25.

(56) Wang, J.; Wolf, R. M.; Caldwell, J. W.; Kollman, P. A.; Case, D. A. Development and testing of a general amber force field. *Journal of Computational Chemistry* **2004**, *25*, 1157–1174.

(57) Huang, J.; Rauscher, S.; Nawrocki, G.; Ran, T.; Feig, M.; de Groot, B. L.; Grubmüller, H.; MacKerell, A. D. CHARMM36M: An improved force field for folded and intrinsically disordered proteins. *Nature Methods* **2016**, *14*, 71–73.

(58) Jorgensen, W. L.; Maxwell, D. S.; Tirado-Rives, J. Development and Testing of the OPLS

All-Atom Force Field on Conformational Energetics and Properties of Organic Liquids. *Journal of the American Chemical Society* **1996**, *118*, 11225–11236.

(59) Jakalian, A.; Jack, D. B.; Bayly, C. I. Fast, efficient generation of high-quality atomic charges. AM1-BCC model: II. Parameterization and validation. *Journal of Computational Chemistry* **2002**, *23*, 1623–1641.

(60) Case, D. A. et al. AmberTools. *Journal of Chemical Information and Modeling* **2023**, *63*, 6183–6191, PMID: 37805934.

(61) Sousa da Silva, A. W.; Vranken, W. F. ACPYPE - AnteChamber PYthon Parser interfacE. *BMC Research Notes* **2012**, *5*.

(62) Essmann, U.; Perera, L.; Berkowitz, M. L.; Darden, T.; Lee, H.; Pedersen, L. G. A smooth particle mesh Ewald method. *The Journal of Chemical Physics* **1995**, *103*, 8577–8593.

(63) Bussi, G.; Donadio, D.; Parrinello, M. Canonical sampling through velocity rescaling. *The Journal of Chemical Physics* **2007**, *126*, 014101.

(64) Bernetti, M.; Bussi, G. Pressure control using stochastic cell rescaling. *The Journal of Chemical Physics* **2020**, *153*, 114107.

(65) Frisch, M. J. et al. Gaussian 09, Revision B.01. 2016.

(66) Bertie, J. E.; Zhang, S. L.; Eysel, H. H.; Baluja, S.; ; Ahmed, M. K. Infrared Intensities of Liquids XI: Infrared Refractive Indices from 8000 to 2 cm1, Absolute Integrated Intensities, and Dipole Moment Derivatives of Methanol at 25°C. *Applied Spectroscopy* **1993**, *47*, 1100–1114.

(67) Falk, M.; Whalley, E. Infrared Spectra of Methanol and Deuterated Methanols in Gas, Liquid, and Solid Phases. *The Journal of Chemical Physics* **1961**, *34*, 1554–1568.

(68) Perakis, F.; De Marco, L.; Shalit, A.; Tang, F.; Kann, Z. R.; Kühne, T. D.; Torre, R.; Bonn, M.; Nagata, Y. Vibrational Spectroscopy and Dynamics of Water. *Chemical Reviews* **2016**, *116*, 7590–7607.

(69) Auer, B. M.; Skinner, J. L. IR and Raman spectra of liquid water: Theory and interpretation. *The Journal of Chemical Physics* **2008**, *128*.

(70) Asbury, J. B.; Steinel, T.; Fayer, M. Vibrational echo correlation spectroscopy probes of hydrogen bond dynamics in water and methanol. *Journal of Luminescence* **2004**, *107*, 271–286.

(71) Reppert, M.; Tokmakoff, A. Computational Amide I 2D IR Spectroscopy as a Probe of Protein Structure and Dynamics. *Annual Review of Physical Chemistry* **2016**, *67*, 359–386.

(72) Chelius, K.; Wat, J. H.; Phadkule, A.; Reppert, M. Distinct electrostatic frequency tuning rates for amide I and amide I vibrations. *The Journal of Chemical Physics* **2021**, *155*, 195101.

(73) Chen, X. G.; Schweitzer-Stenner, R.; Krimm, S.; Mirkin, N. G.; Asher, S. A. N-Methylacetamide and Its Hydrogen-Bonded Water Molecules Are Vibrationally Coupled. *Journal of the American Chemical Society* **1994**, *116*, 11141–11142.

(74) Golonzka, O.; Tokmakoff, A. Polarization-selective third-order spectroscopy of coupled vibronic states. *The Journal of Chemical Physics* **2001**, *115*, 297–309.

(75) Tokmakoff, A. Orientational correlation functions and polarization selectivity for nonlinear spectroscopy of isotropic media. I. Third order. *The Journal of Physical Chemistry* **1996**, *105*, 1–12.

(76) Hochstrasser, R. M. Two-dimensional IR-spectroscopy: polarization anisotropy effects. *Chemical Physics* **2001**, *266*, 273–284.

(77) Hayashi, T.; Mukamel, S. Correlated hydrogen bonding fluctuations and vibrational cross peaks in N-methyl acetamide: Simulation based on a complete electrostatic density functional theory map. *The Journal of Chemical Physics* **2006**, *125*, 194510.

(78) Torii, H.; Tasumi, M. Charge Fluxes and Changes in Electronic Structures as the Origin of Infrared Intensities in the Ground and Excited Electronic States. *The Journal of Physical Chemistry B* **1997**, *101*, 466–471.

(79) Torii, H.; Tatsumi, T.; Tasumi, M. Effects of hydration on the structure, vibrational wavenumbers, vibrational force field and resonance raman intensities of N-methylacetamide. *Journal of Raman Spectroscopy* **1999**, *29*.

(80) Geissler, P. L. Water interfaces, solvation, and spectroscopy. *Annual Review of Physical Chemistry* **2013**, *64*, 317–337.

(81) Eaves, J. D.; Tokmakoff, A.; Geissler, P. L. Electric Field Fluctuations Drive Vibrational Dephasing in Water. *The Journal of Physical Chemistry A* **2005**, *109*, 9424–9436.

(82) Corcelli, S. A.; Lawrence, C. P.; Skinner, J. L. Combined electronic structure/molecular dynamics approach for ultrafast infrared spectroscopy of dilute HOD in liquid H2O and D2O. *The Journal of Chemical Physics* **2004**, *120*, 8107–8117.

(83) Torii, H. Amide I Vibrational Properties Affected by Hydrogen Bonding Out-of-Plane of the Peptide Group. *The Journal of Physical Chemistry Letters* **2015**, *6*.

(84) Remko, M.; Sekerka, I.; Frecer, V. Quantum-chemical study of N-methylacetamide and N,N-dimethylacetamide as models for peptidic bond in hydrogen-bond interaction with water, methanol and phenol. *Collection of Czechoslovak Chemical Communications* **1983**, *48*, 3214–3222.

(85) Takahashi, F.; Li, N. Proton Magnetic Resonance Studies of Hydrogen Bonding of 2-

Propanol with N-Methylacetamide and , N,N'-Dimethylacetamide. *The Journal of Physical Chemistry* **1964**, *68*, 2136–2140.

(86) Baiz, C. R. et al. Vibrational Spectroscopic Map, Vibrational Spectroscopy, and Intermolecular Interaction. *Chemical Reviews* **2020**, *120*, 7152–7218.

(87) Tucker, M. J.; Mallon, C. J.; Hassani, M. The Long and Short of Coupling and Uncoupling via 2D IR Spectroscopy. *The Journal of Physical Chemistry B* **2024**, *129*, 1439–1452.

(88) Tokmakoff, A. Time-Dependent Quantum Mechanics and Spectroscopy. 2014; `https://tdqms.uchicago.edu/`.

(89) Buchner, T. F.; Sato, T.; Watanabe, J.; Hama, Y.; Kunz, W.; Richard Relation between Dielectric and Low-Frequency Raman Spectra of Hydrogen-Bond Liquids. *Physical Review Letters* **2005**, *95*.

(90) Tobias Kampfrath, M. W., R. Kramer Campen; Sajadi, M. The Nature of the Dielectric Response of Methanol Revealed by the Terahertz Kerr Effect. *The Journal of Physical Chemistry Letters* **2018**, *9*, 1279–1283.

(91) Petersen, P. B.; Roberts, S. T.; Ramasesha, K.; Nocera, D. G.; Tokmakoff, A. Ultrafast N-H Vibrational Dynamics of Cyclic Doubly Hydrogen-Bonded Homo- and Heterodimers. *Journal of Physical Chemistry B* **2008**, *112*, 13167–13171.

(92) Marco, L. D. The Molecular Dynamics of Hydrogen-Bonding Explored with Broadband Two Dimensional Infrared Spectroscopy. Thesis, 2016.

(93) Jr, K. K.; Kawato, S.; Ikegami, A. A theory of fluorescence polarization decay in membranes. *Biophysical Journal* **1977**, *20*, 289–305.

(94) Lipari, G.; Szabo, A. Effect of librational motion on fluorescence depolarization and nuclear magnetic resonance relaxation in macromolecules and membranes. *Biophysical Journal* **1980**, *30*, 489–506.

(95) Li, Z.; Wang, J.; Li, Y.; Xiong, W. Solving the "Magic Angle" Challenge in Determining Molecular Orientation Heterogeneity at Interfaces. *The Journal of Physical Chemistry C* **2016**, *120*, 20239–20246.

(96) Vinaykin, M.; Benderskii, A. V. Orientational Dynamics in Sum Frequency Spectroscopic Line Shapes. *The Journal of Physical Chemistry B* **2013**, *117*.

(97) Nishida, J.; Fayer, M. D. Theory of third-order spectroscopic methods to extract detailed molecular orientational dynamics for planar surfaces and other uniaxial systems. *The Journal of Chemical Physics* **2014**, *140*, 144702.

(98) Ukawa, H. T.; Ryota Role of Intermolecular Charge Fluxes in the Hydrogen-Bond-Induced Frequency Shifts of the OH Stretching Mode of Water. *The Journal of Physical Chemistry B* **2021**, *125*, 1468–1475.

(99) Novak, A. *Hydrogen bonding in solids correlation of spectroscopic and crystallographic data*; Springer Berlin Heidelberg, pp 177–216.

(100) Torii, H. Intermolecular charge fluxes and terahertz spectral features of liquid methanol. *Journal of Molecular Liquids* **2023**, *390*.

(101) De Marco, L.; Fournier, J. A.; Thämer, M.; Carpenter, W.; Tokmakoff, A. Anharmonic exciton dynamics and energy dissipation in liquid water from two-dimensional infrared spectroscopy. *The Journal of Chemical Physics* **2016**, *145*, 094501.

(102) Fecko, C. J.; Eaves, J. D.; Loparo, J. J.; Tokmakoff, A.; Geissler, P. L. Ultrafast Hydrogen-Bond Dynamics in the Infrared Spectroscopy of Water. *Science* **2003**, *301*, 1698–1702.

(103) Nibbering, E. T. J.; Elsaesser, T. Ultrafast Vibrational Dynamics of Hydrogen Bonds in the Condensed Phase. *Chemical Reviews* **2004**, *104*, 1887–1914.

(104) Gündoğdu, K.; Bandaria, J.; Nydegger, M.; Rock, W.; Cheatum, C. M. Relaxation and

anharmonic couplings of the O–H stretching vibration of asymmetric strongly hydrogen-bonded complexes. *The Journal of Chemical Physics* **2007**, *127*, 044501.

(105) Elsaesser, T.; Huse, N.; Dreyer, J.; Dwyer, J. R.; Heyne, K.; Nibbering, E. T. Ultrafast vibrational dynamics and anharmonic couplings of hydrogen-bonded dimers in solution. *Chemical Physics* **2007**, *341*, 175–188.

(106) Fournier, J. A.; Carpenter, W. B.; Lewis, N. H. C.; Tokmakoff, A. Broadband 2D IR spectroscopy reveals dominant asymmetric H5O2+ proton hydration structures in acid solutions. *Nature Chemistry* **2018**, *10*, 932–937.

(107) Lippincott, E. R.; Schroeder, R. One-Dimensional Model of the Hydrogen Bond. *The Journal of Chemical Physics* **1955**, *23*, 1099–1106.

(108) Rudolph Schroeder, E. R. L. Potential Function Model of Hydrogen Bonds. II. *The Journal of Physical Chemistry* **1957**, *61*, 921–928.

(109) Bowman, Q. Y.; M., J. High-Level Quantum Calculations of the IR Spectra of the Eigen, Zundel, and Ring Isomers of H+(H2O)4 Find a Single Match to Experiment. *Journal of the American Chemical Society* **2017**, *139*, 10984–10987.

(110) Torii, H. Electrostatic origin of the cooperative effect on the C6-point double bondO bond lengths and the amide I vibrational frequencies of the N-methylacetamide oligomers. *Journal of Molecular Structure* **2005**, *735-736*, 21–26.

(111) Baronio, C. M.; Barth, A. The Amide I Spectrum of Proteins—Optimization of Transition Dipole Coupling Parameters Using Density Functional Theory Calculations. *The Journal of Physical Chemistry B* **2020**,

(112) Donaldson, P. M. Spectrophotometric Concentration Analysis Without Molar Absorption Coefficients by Two-Dimensional-Infrared and Fourier Transform Infrared Spectroscopy. *Analytical Chemistry* **2022**, *94*, 17988–17999.

(113) Jonas, B. C.; Tiwari, V.; M., D. Simultaneous All-Optical Determination of Molecular Concentration and Extinction Coefficient. *Analytical Chemistry* **2013**, *85*, 5514–5521.

(114) Grechko, M.; Zanni, M. T. Quantification of transition dipole strengths using 1D and 2D spectroscopy for the identification of molecular structures via exciton delocalization: Application to -helices. *The Journal of Chemical Physics* **2012**, *137*, 184202.

(115) Moilanen, D. E.; Wong, D.; Rosenfeld, D. E.; Fenn, E. E.; Fayer, M. D. Ion–water hydrogen-bond switching observed with 2D IR vibrational echo chemical exchange spectroscopy. *Proceedings of the National Academy of Sciences* **2009**, *106*, 375–380.

(116) Baiz, S. C. E.; Flanagan, J. C.; R., C. An Empirical IR Frequency Map for Ester CO Stretching Vibrations. *The Journal of Physical Chemistry A* **2016**, *120*, 3888–3896.

(117) Chuntonov, L.; Pazos, I. M.; Ma, J.; Gai, F. Kinetics of Exchange between Zero-, One-, and Two-Hydrogen-Bonded States of Methyl and Ethyl Acetate in Methanol. *The Journal of Physical Chemistry B* **2015**, *119*, 4512–4520.

(118) Bhatta, R. S.; Iyer, P. P.; Dhinojwala, A.; Tsige, M. A brief review of Badger–Bauer rule and its validation from a first-principles approach. *Modern Physics Letters B* **2014**, *28*, 1430014.

(119) Santis, G. D.; Xantheas, S. S. Extending Badger's rule. I. The relationship between energy and structure in hydrogen bonds. *The Journal of Chemical Physics* **2025**, *162*.

(120) Santis, G. D.; Xantheas, S. S. Extending Badger's rule. II. The relationship between energy and vibrational spectra in hydrogen bonds. *The Journal of Chemical Physics* **2025**, *162*.

(121) Carmella Calabrese, L. S., Ashley M. Stingel; Petersen, P. B. Ultrafast continuum mid-infrared spectroscopy: probing the entire vibrational spectrum in a single laser shot with femtosecond time resolution. *Optics Letters* **2012**, *37*, 2265–2267.